



Identification of neural oscillations and epileptiform changes in human brain organoids

Ranmal A. Samarasinghe^{1,2,3,4}, Osvaldo A. Miranda^{1,3,4}, Jessie E. Buth^{1,3,4}, Simon Mitchell^{5,6}, Isabella Ferando², Momoko Watanabe^{1,3,4,17}, Thomas F. Allison^{3,7}, Arinnae Kurdian^{1,3,4,8}, Namie N. Fotion^{1,3,4}, Michael J. Gandal^{4,9}, Peyman Golshani^{1,2,4,10,11}, Kathrin Plath^{1,3,7}, William E. Lowry^{1,3,12}, Jack M. Parent^{1,3,14,15}, Istvan Mody^{2,16} and Bennett G. Novitch^{1,3,4}✉

Brain organoids represent a powerful tool for studying human neurological diseases, particularly those that affect brain growth and structure. However, many diseases manifest with clear evidence of physiological and network abnormality in the absence of anatomical changes, raising the question of whether organoids possess sufficient neural network complexity to model these conditions. Here, we explore the network-level functions of brain organoids using calcium sensor imaging and extracellular recording approaches that together reveal the existence of complex network dynamics reminiscent of intact brain preparations. We demonstrate highly abnormal and epileptiform-like activity in organoids derived from induced pluripotent stem cells from individuals with Rett syndrome, accompanied by transcriptomic differences revealed by single-cell analyses. We also rescue key physiological activities with an unconventional neuroregulatory drug, pifithrin- α . Together, these findings provide an essential foundation for the utilization of brain organoids to study intact and disordered human brain network formation and illustrate their utility in therapeutic discovery.

Brain organoids derived from human embryonic stem cells (hESCs) and human induced pluripotent stem cells (hiPSCs) recapitulate unique features of human brain development and are increasingly being used as model systems to gain new insights into a variety of neurological diseases^{1–3}. Organoids represent a notable advance in the toolkit available for understanding human brain function and disease mechanisms, as much of our current knowledge is derived from studies of embryonic and adult animals, particularly rodents. While there is conservation in many mechanisms of brain development across evolution, it has become increasingly clear that the human brain nevertheless possesses distinct features^{4,5}, and it remains unclear how well animal models of neurological disease faithfully recapitulate human pathologies. Moreover, drugs shown to be effective in ameliorating neurological disease in animals frequently fail in clinical trials^{6,7}, emphasizing the need for human cell-based systems to evaluate drug efficacy.

Most brain organoid studies to date have capitalized on the anatomical and cytoarchitectural characteristics of organoids to model disorders that grossly impact human brain growth or organization such as microcephaly, macrocephaly and lissencephaly^{1–3}. However, the diverse functions of the human brain depend not only on its stereotyped anatomical structure, but also on the establishment and

function of neural networks. Indeed, errors in the formation of these circuits or damage after their development are thought to underlie many neurological diseases ranging from autism and neuropsychiatric disorders to epilepsy and Alzheimer's disease^{8,9}. Reliably assessing network activity becomes especially critical in situations in which there is clear clinical disease but no overt structural brain abnormality.

Despite evidence of the enhanced organizational complexity of brain organoids relative to other *in vitro* systems, the presence of sophisticated neural network activities has only recently been demonstrated in live whole-organoid preparations^{10,11}. A key feature of robust neural networks is the presence of distinct frequencies of oscillatory activity. Such activities are thought to depend on precisely tuned inhibitory–excitatory neuronal interactions and can be recorded from intact and sliced brain preparations, but are not readily achievable in two-dimensional culture systems^{12,13}. In addition, specific changes in oscillatory activity, such as the loss of gamma rhythms or the emergence of polymorphic low-frequency activity, can be clear indicators of underlying neurological dysfunction^{14–16}.

Here, we sought to develop and characterize brain organoid network activity, utilizing recent advances in organoid techniques¹⁷ to generate cerebral cortex–ganglionic eminence (Cx+GE) ‘fusion’

¹Department of Neurobiology, David Geffen School of Medicine at UCLA, Los Angeles, CA, USA. ²Department of Neurology, David Geffen School of Medicine at UCLA, Los Angeles, CA, USA. ³Eli and Edythe Broad Center for Regenerative Medicine and Stem Cell Research, University of California, Los Angeles, Los Angeles, CA, USA. ⁴Intellectual Development and Disabilities Research Center, David Geffen School of Medicine at UCLA, Los Angeles, CA, USA. ⁵Institute for Quantitative and Computational Biosciences, Department of Microbiology, Immunology, and Molecular Genetics, University of California, Los Angeles, Los Angeles, CA, USA. ⁶Brighton and Sussex Medical School, Falmer, United Kingdom. ⁷Department of Biological Chemistry, David Geffen School of Medicine at UCLA, Los Angeles, CA, USA. ⁸CIRM CSUN-UCLA Stem Cell Training Program, California State University, Northridge, CA, USA. ⁹Department of Psychiatry and Biobehavioral Sciences, David Geffen School of Medicine at UCLA, Los Angeles, CA, USA. ¹⁰Semel Institute for Neuroscience and Human Behavior, University of California, Los Angeles, Los Angeles, CA, USA. ¹¹West Los Angeles VA Medical Center, Los Angeles, CA, USA. ¹²Department of Molecular, Cell, and Developmental Biology, University of California, Los Angeles, Los Angeles, CA, USA. ¹³Department of Neurology, University of Michigan Medical School, Ann Arbor, MI, USA. ¹⁴Michigan Neuroscience Institute, University of Michigan, Ann Arbor, MI, USA. ¹⁵Ann Arbor VA Healthcare System, University of Michigan Medical School, Ann Arbor, MI, USA. ¹⁶Department of Physiology, David Geffen School of Medicine at UCLA, Los Angeles, CA, USA. ¹⁷Present address: Department of Anatomy & Neurobiology, Sue & Bill Gross Stem Cell Research Center, School of Medicine, University of California, Irvine, Irvine, CA, USA. ✉e-mail: bnovitch@ucla.edu

organoids in which excitatory and inhibitory neurons functionally integrate^{18–20}. We then used a combination of calcium sensor imaging and extracellular recordings of local field potentials (LFPs) to demonstrate the presence of intricate network-level activities, including oscillatory rhythms. This work builds on prior approaches that analyzed network activity in cortical organoids using either calcium indicator imaging alone or plate-based multi-electrode recordings^{10,11,17,21}. The advances encompassed by the present techniques allowed us to clearly discern pathological network and oscillatory changes in fusion organoids containing mutations in the methyl-CpG binding protein 2 (*MECP2*) gene associated with Rett syndrome²². Consistent with broadly similar patterns of clinical electroencephalographic abnormalities between individuals with mutations in *MECP2* as well as instances of between-person variability^{23,24}, we identified conserved physiological changes across organoids generated from multiple hiPSC lines derived from two individuals, as well as some physiological activities distinct to each person. In both cases, neural network dysfunction was partially rescued by treatment with an unconventional neuroregulatory drug, Pifithrin- α . Collectively, these findings provide a framework for how brain organoids can be utilized to investigate network-level functions of the human brain and illustrate their utility in modeling neurological disorders and therapeutic testing.

Results

Excitatory and inhibitory neuron integration within organoids. As cortical circuits *in vivo* contain a mixture of both excitatory and inhibitory connections, we sought to replicate this process using an organoid ‘fusion’ technique to combine separately generated cortical and subcortical organoids and thereby create integrated structures (Fig. 1). Organoids derived from either H9 hESC or wild-type iPSC lines were directed towards Cx or GE identities through the absence or presence of Sonic hedgehog (Shh) pathway agonists in the organoid differentiation scheme (Fig. 1a)¹⁷. Without Shh signaling, organoids exhibited cortical characteristics including expression of the apical and basal radial glial progenitor marker PAX6, the intermediate progenitor marker TBR2 (encoded by *EOMES*), deep cortical plate markers including TBR1, CTIP2 (encoded by *BCL11B*) and BHLHB5 (encoded by *BHLHE22*), and superficial layer markers such as SATB2 and BRN2 (encoded by *POU3F2*; Fig. 1b and refs. ^{17,25}). Shh pathway-stimulated organoids by contrast expressed canonical GE progenitor and migratory interneuron markers such as NKX2.1, DLX1, DLX2 and OLIG2. Over time in culture, many neurons within GE organoids expressed GABAergic inhibitory neuron markers such as GAD65 (encoded by *GAD2*) and GABA along with a variety of interneuron subtype markers (Fig. 1b, see also refs. ^{17,25}).

In the developing forebrain *in vivo*, GE-derived interneurons migrate tangentially into the adjacent Cx and functionally integrate into cortical neural networks, a process that can be recapitulated *in vitro*^{18–20}. Using adeno-associated virus (AAV) CAG:tdTomato labeling of the GE organoid before Cx + GE fusion, we observed widespread migration of tdTomato⁺ cells from the GE and

dispersion within the adjacent Cx such that at 2 weeks after fusion ~18% of Cx cells were tdTomato positive (Fig. 1a,c and Extended Data Fig. 1a,d). Minimal tdTomato⁺ cell migration was seen in control Cx + Cx or Cx + GE fusions where Cx was prelabeled with AAV-tdTomato. There was a high degree of reproducibility in the colonization of the Cx compartment by inhibitory interneurons, which on average resulted in a final percentage of ~25% of cells being GABAergic (Figs. 1d and 3c,d), on par with the 20–30% density seen in the mammalian neocortex *in vivo*^{26,27}. This number also appeared consistent across organoid batches (Extended Data Fig. 1a,b).

Immunohistochemical analyses of the cortical aspect of Cx + GE fusions revealed intermingling of Cx-derived excitatory neurons, exemplified by SATB2, which is not expressed within GE organoids, and inhibitory interneurons identified by GAD65 and DLX5 co-staining (Fig. 1d). By contrast, Cx + Cx fusions only expressed the neuronal marker SATB2 with few if any GAD65⁺DLX5⁺ cells (Fig. 1d). Integration of excitatory and inhibitory interneurons within Cx + GE organoids was further confirmed by the prominence of both excitatory synapses, distinguished by apposed VGLUT1⁺ presynaptic and PSD95⁺ postsynaptic puncta, and inhibitory synapses visualized by VGAT and GEPHYRIN staining (Fig. 1e). By comparison, Cx + Cx organoids mainly contained only excitatory synaptic puncta (Fig. 1e), indicating that most inhibitory synapses in the Cx + GE organoids are GE derived.

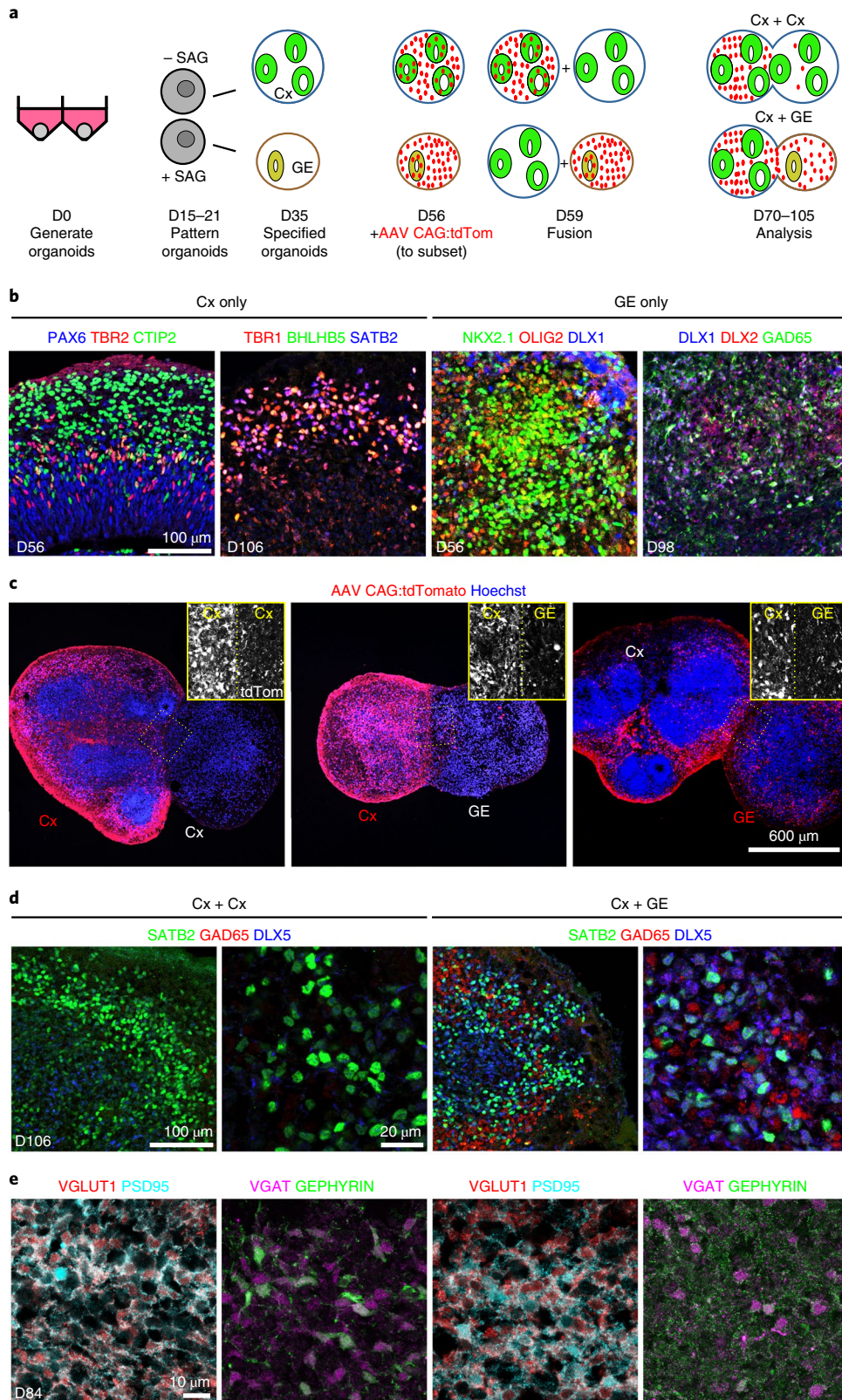
Cx + GE organoids exhibit complex neural network oscillations. To determine the range of physiological activity in the fusion organoids, we utilized both live two-photon microscopy-based calcium indicator imaging of intact organoids and extracellular recordings of LFPs (Fig. 2a). In accordance with existing *ex vivo* slice recording protocols, LFP recordings and calcium imaging were performed in the presence of low levels of kainate sufficient to induce oscillations yet not evoke seizure-like hyperexcitability²⁸. We applied constrained nonnegative matrix factorization extended (CNMF-E) methods for calcium signal processing to extract spiking dynamics from records^{29,30}. This enabled us to perform unbiased categorization of single-cell calcium dynamics into functional microcircuit clusters (Extended Data Fig. 2, Supplementary Fig. 1 and Supplementary Videos 1–3). In combination with LFP data, this approach allowed us to characterize brain organoid physiological activity at single-cell, microcircuit and network levels.

After infection with AAV1 Syn:GCaMP6f virus, we measured spontaneous calcium activity as changes in GCaMP6f fluorescence ($\Delta F/F$, Fig. 2b). Both Cx + Cx and Cx + GE fusions showed comparable baseline neural activities (Fig. 2c and Supplementary Fig. 1). However, when we assessed the role of inhibition by adding either the GABA_A receptor antagonist bicuculline methiodide (BMI) or gabazine, only Cx + GE fusions showed functional connectivity between GABAergic interneurons and glutamatergic cells. Both drugs elicited repetitive waves of nearly complete synchronization of calcium transients in Cx + GE fusions (Fig. 2c,d), with no such

Fig. 1 | Generation and characterization of fusion brain organoids. **a**, Schematic outlining the generation, patterning and fusion of dorsal Cx and ventral GE organoids. +SAG indicates administration of Smoothened Agonist to stimulate the ventralizing activity of the Shh pathway. **b**, Immunohistochemical analysis of H9 hESC-derived or nonmutant hiPSC-derived Cx and GE organoids before fusion at the indicated days (D) of differentiation *in vitro*. **c**, Before fusion, D56 Cx or GE organoids were infected with AAV1-CAG:tdTomato virus, allowing for tracking of cells emanating from each compartment. Two weeks after fusion, labeled Cx cells showed limited migration into adjacent Cx or GE structures (left and middle), while labeled GE progenitors displayed robust migration and colonization of their Cx partner (right). **d**, Immunohistochemical analysis showing intermingling of SATB2⁺ cortical neurons with DLX5⁺GAD65⁺ inhibitory interneurons in the cortical compartment of D106 Cx + GE but not Cx + Cx fusion organoids. **e**, At D84, Cx + Cx fusions (left) contained numerous excitatory synapses reflected by prominent colocalization of the presynaptic and postsynaptic markers VGLUT1 and PSD95, respectively, yet sparse numbers of inhibitory synapses were detected by VGAT and GEPHYRIN co-staining. Cx + GE fusions (right) on the other hand contained numerous VGLUT1⁺/PSD95⁺ excitatory and VGAT⁺/GEPHYRIN⁺ inhibitory synapses (right). All images in **b–e** are representative of multiple experiments and represent one of at least three or more imaged sections. For specific details, see Supplementary Table 4.

effect in Cx + Cx fusions (Fig. 2c–e and Supplementary Videos 4–7). Hierarchical clustering revealed large groups of neurons with highly correlated activity in Cx + GE organoids following BMI treatment, while only small groups were observed in the Cx + Cx organoids (Fig. 2d).

LFP measurements in untreated fusion organoids uncovered simultaneous sustained oscillations at multiple frequencies from 1–100 Hz in Cx + GE fusions (Fig. 2f–h), a hallmark of mature neural networks in vivo³¹. No discernible oscillatory activities were seen in Cx + Cx structures (Fig. 2i–k). These findings suggested that the



presence of GE-derived inhibitory interneurons stimulates maturation of excitatory cortical networks, as has been shown in the rodent brain^{32,33}. Moreover, these data indicated that interneurons uniquely entrain the behavior of excitatory cells in Cx + GE fusions, and that the resultant networks could produce complex oscillations resembling those observed by extracranial and intracranial recordings of the intact brain.

Generation of Cx + GE fusion organoids to model Rett syndrome. We next used this platform to measure pathophysiological changes associated with human neurological disease. Rett syndrome is a neurodevelopmental disorder typically caused by de novo mutations in one copy of the *MECP2* gene on the X chromosome, where affected females exhibit symptoms including motor delays, cognitive and neuropsychiatric disturbances, autism and epilepsy as early as 7 months of age³⁴. However, cellular defects likely present well before clinical symptoms. For example, a recent hiPSC-based study suggested that Rett may impact prenatal neurogenesis through microRNA-mediated alterations in AKT and ERK pathway activity³⁵. While neuroanatomical changes in dendritic arborization and spine density have been reported in multiple Rett models^{34,36–39}, gross structural brain abnormalities are less prevalent.

Due to random X-chromosome inactivation, females with Rett syndrome are typically mosaic in their *MECP2* status, with some cells expressing and others lacking a functional *MECP2* allele. This feature permitted the isolation of isogenic hiPSC pairs from individuals as hiPSC reprogramming does not typically revert X-chromosome silencing³⁹. We accordingly generated Cx and GE organoids from isogenic control (iCtrl) and *MECP2*-mutant (Mut) hiPSCs from two individuals with Rett syndrome harboring either a 705ΔG mutation, which leads to a frameshift truncation after amino acid 236, or a 1461 A>G missense mutation, which alters the C-terminal end of the *MECP2* protein³⁹. The former individual was reported to have a history of electroencephalographic abnormalities and the latter had a documented history of overt seizures. We confirmed that the expected *MECP2*-positive or *MECP2*-negative status of cells was retained following differentiation using immunohistochemistry and found no obvious differences in organoid cytoarchitecture or cell composition across samples (Fig. 3a,b and Extended Data Figs. 3 and 4a).

We next examined the interneuron composition of fusion organoids made from the first individual (harboring a 705ΔG mutation) in greater detail. The Cx regions of both iCtrl and Mut Cx + GE fusions were indistinguishable with respect to migration of AAV1-CAG:tdTomato-labeled GE-derived cells in the cortical compartment and contained similar percentages of GAD65⁺ interneurons (mean ~25% of all cells; Fig. 3c,d, Extended Fig. 1a,b and Supplementary Figs. 2a,b). Immunohistochemical analyses revealed the presence of multiple interneuron subtypes in all fusion organoids including cells expressing somatostatin (SST), calretinin

(CALB2), neuropeptide Y (NPY) and calbindin (CALB1). The percentage of CALB2-, CALB1- and NPY-positive groups appeared slightly elevated in the Mut samples, while the percentage of SST was down; however, most changes were modest and did not achieve statistical significance except for calretinin (Fig. 3e,f).

Neurogenesis and fate changes in *MECP2*-mutant Cx + GE organoids. To obtain a more comprehensive profile of the cell composition within the Mut and iCtrl fusion organoids, we performed single-cell RNA sequencing (scRNA-seq) on pre-fusion D56 Cx and GE organoids as well as D70 and D100 Cx + GE fusions. Multiple time points were selected to assess the progression of cells from progenitor to differentiated states. Uniform manifold approximation and projection (UMAP) clustering revealed nine clusters that expressed cell-type-specific markers including ventricular radial glial cells, outer radial glia cells, excitatory neurons (upper layer callosal projection neurons (CPNs) and deep layer corticofugal projection neurons (CFuPNs)) and inhibitory interneurons (Fig. 4a,b and Supplementary Table 1). We plotted the expression of canonical markers associated with each of these clusters (for example, *GAD1* with interneurons or *SATB2* with excitatory clusters), including many of the markers we had used for immunohistochemical analyses of neuronal subtypes (Fig. 4c and Supplementary Fig. 3). Genes associated with astrocyte progenitors and maturing astrocytes (for example, *GFAP*, *FGFR3*, *AQP4* and *ALDH1L1*) overlapped with the outer radial glia cluster (Fig. 4a,c and Supplementary Fig. 3) but did not further separate into a distinct astrocyte cluster, reflecting the high degree of similarity in gene expression between these cell types.

To identify the effects of *MECP2* mutations on gene expression and cell fates, we performed differential expression analysis between all cells in the iCtrl and Mut organoids, and when separated by clusters. We found broadly overlapping gene expression profiles, with a trend toward an increased percentage of cells exhibiting progenitor characteristics in iCtrl fusion organoids compared to Mut samples (Fig. 4b). Although both progenitor and mature cell types were seen at all time points, the data showed a shift from more immature cell-type profiles in day 56 and 70 organoids, to more mature cell types such as CPNs in the D100 samples. This shift appeared sooner in the *MECP2*-mutant samples (Supplementary Fig. 3a).

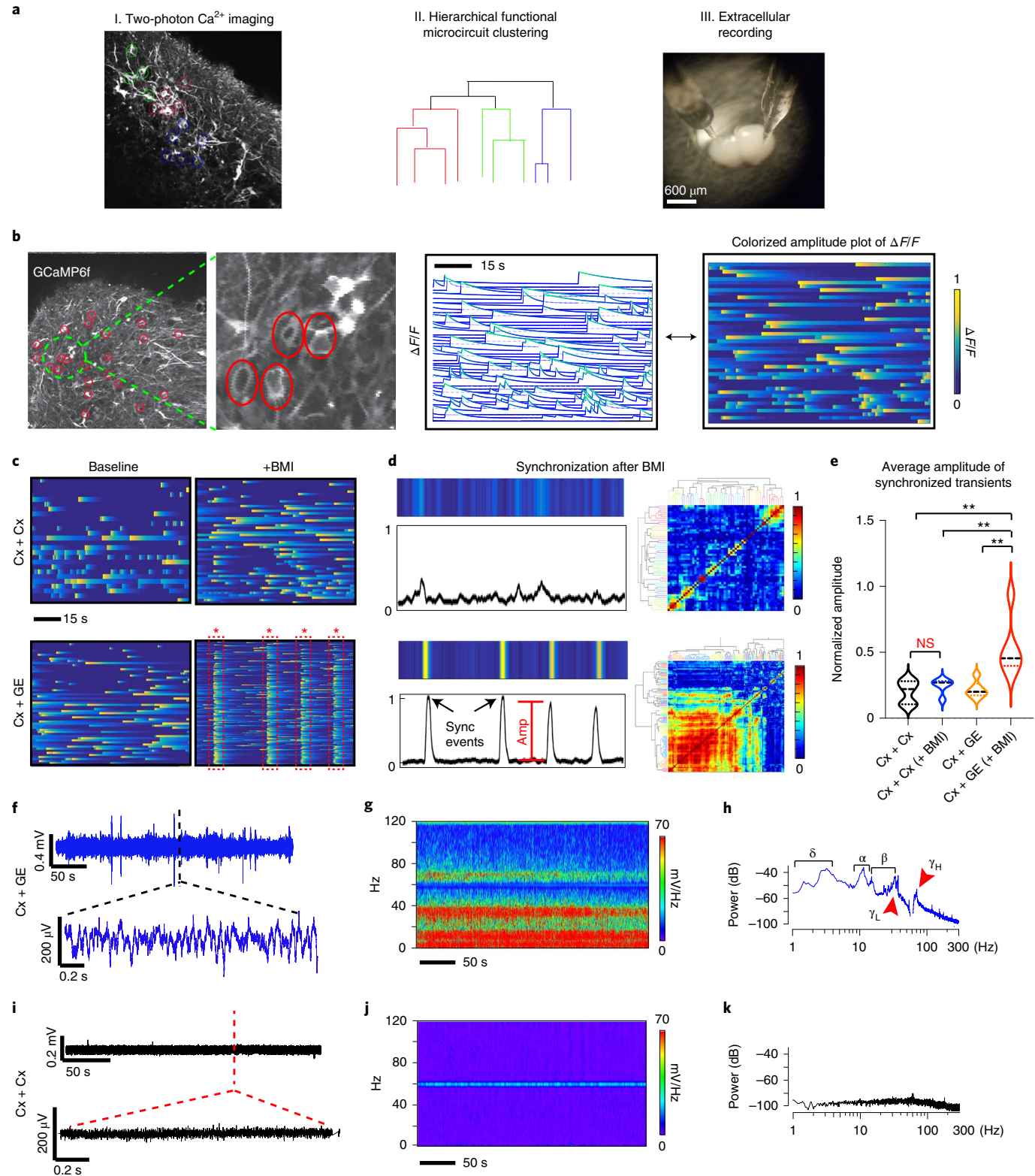
Given the importance of interneuron function for neural oscillations in the fusion organoids, we isolated the inhibitory neuron population from Fig. 4a to further distinguish interneuron subtypes. We found seven major subclusters defined by their distinct profile of interneuron-associated genes such as *SST*, *NPY*, *CALB1* and *CALB2*, vasoactive intestinal polypeptide (encoded by *VIP*) and parvalbumin (encoded by *PVALB*), and variable expression of additional genes such as *DLX2*, *DLX5*, *GAD2*, *SLC6A1*, *SLC32A1*, *LAMP5*, *SCGN* and *TAC1* (Fig. 4d–f). While all interneuron groups were present in iCtrl and Mut fusion organoids, there were some modest yet notable differences in cell numbers. iCtrl samples

Fig. 2 | Cx + GE fusion organoids demonstrate complex neural network activities including oscillatory rhythms. **a**, Schematic illustrating the identification of active neurons by virtue of their Ca²⁺ transients (I), representation of their network organization (II) and methods used to collect extracellular recordings (III). **b**, Example of live two-photon microscopy imaging of an H9 hESC-derived fusion organoid demonstrating acquisition of regions of interest (red circles) and the resulting activity profile shown as normalized ΔF/F values, where each line is an individual neuron (middle) and representation of the same data as a colorized amplitude plot (right). **c**, Addition of 100 μM BMI had a minimal effect on Cx + Cx fusions (top) yet elicited spontaneous synchronization of neural activities in Cx + GE organoids (bottom). **d**, These synchronizations can be transformed into a normalized amplitude-versus-time plot for quantitative analyses (left) and further visualized as a clustergram following hierarchical clustering of calcium spiking data (right). **e**, Pooled data of the amplitude measurements. Plots display the full distribution of individual data points. Dashed and dotted lines indicate the median and quartile values, respectively. *n*=3 independent experiments for Cx + Cx and Cx + GE. Analysis of variance (ANOVA) *P*=0.0011, *F*=8.301, d.f. (between columns)=3 followed by Tukey's multiple-comparison test; ***P*=0.0028 for Cx + Cx versus Cx + GE BMI; ***P*=0.0100 for Cx + Cx BMI versus Cx + GE BMI; ***P*=0.0031 for Cx + GE versus Cx + GE BMI. **f–h**, LFPs measured from a representative Cx + GE fusion revealed robust oscillatory activities at multiple frequencies during a 5-min period, reflected in both raw traces (**f**) and the spectrogram (**g**). Spectral density analysis in **h** demonstrates the presence of multiple distinct oscillatory peaks ranging from ~1–100 Hz. **i–k**, Cx + Cx fusion organoids by contrast lack measurable oscillatory activities. Representative traces in **f–h** are taken from three independent experiments and in **i–k** from four independent experiments. NS, not significant.

showed an increased percentage of *PVALB*⁺/*SST*⁺ and *CALB1*⁺ neurons, while the Mut samples contained more *VIP*⁺ and *CALB2*⁺ cells (Fig. 4e).

MECP2-mutant organoids show defects in synapse formation. We next performed differential gene expression analyses comparing iCtrl and Mut fusion organoids both in total and within each cell

grouping (Supplementary Table 2). Genes upregulated in Mut versus iCtrl (total cells) were strongly enriched for autism risk (34% concordance with the SFARI Human Gene Module) and epilepsy (20% concordance with the DisGeNET Epilepsy dataset C0014544), and included four genes, *MEF2C*, *GRIA2*, *SMC1A* and *ZBTB18*, where mutations have previously been connected to Rett syndrome-like neurodevelopmental phenotypes (Extended Data Figs. 5 and 6a)^{40–44}.



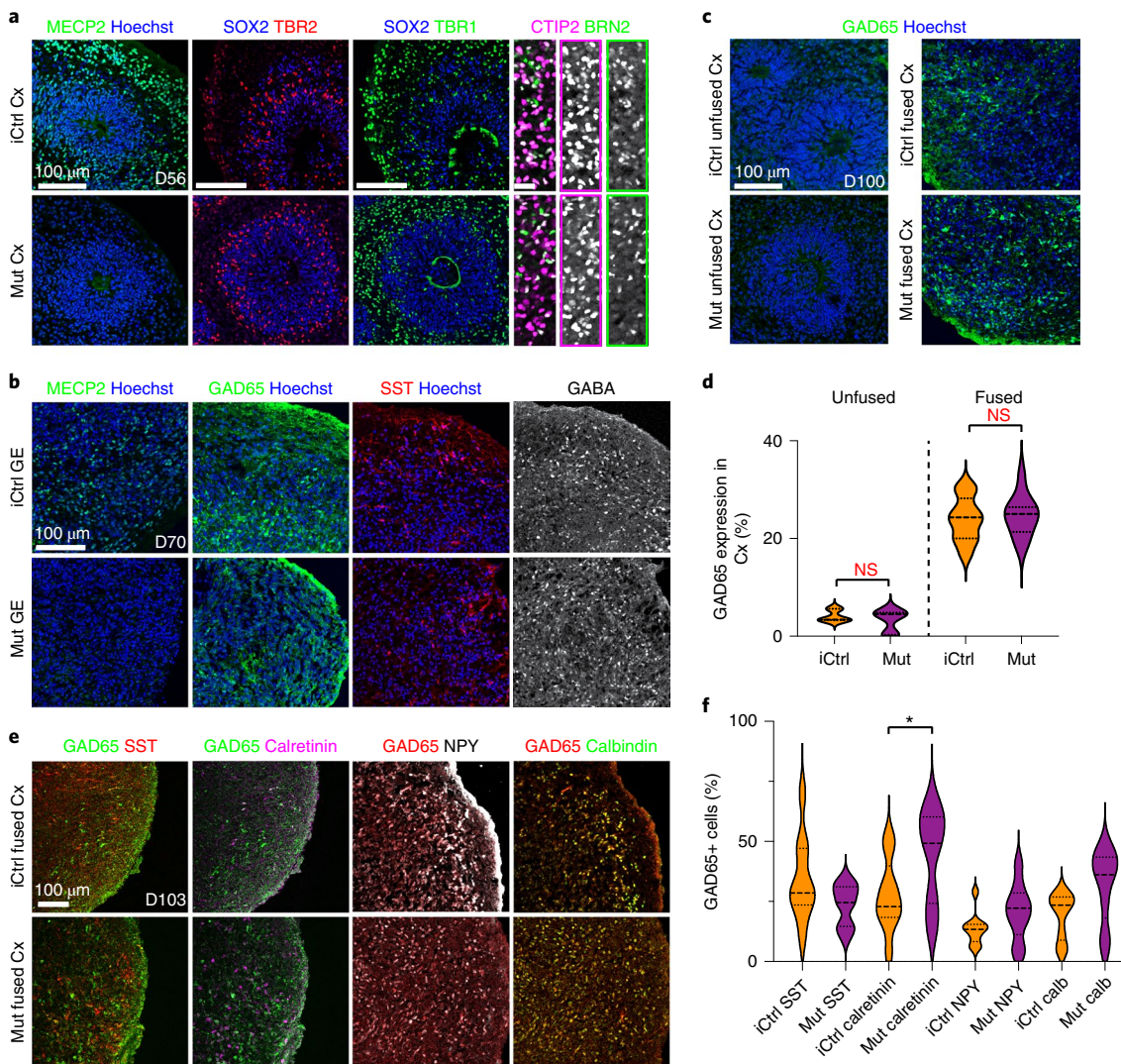


Fig. 3 | Rett syndrome fused and unfused organoids have similar cortical organization and cell-type expression profiles. **a,b**, Generation and immunohistochemical analyses of isogenic Cx and GE organoids from hiPSCs from individuals with Rett syndrome who either contain (iCtrl) or lack (Mut) MECP2 expression³⁹. iCtrl and Mut Cx organoids exhibited comparable formation of neural progenitors (SOX2 and TBR2), neurons of both deep and superficial layers (CTIP2 and BRN2) and inhibitory interneurons (GAD65, SST and GABA). All images are representative of at least three independently imaged sections; see Supplementary Table 4 for further details. **c,d**, D100 unfused iCtrl and Mut Cx organoids showed minimal expression of GAD65, whereas ~20–25% of the cells in the Cx end of age-matched Cx + GE organoids expressed GAD65; $n=3$ independently generated organoids (2,631 cells; NS by a two-sided t-test). **e,f**, Immunohistochemical analysis of interneuron subtypes by the coexpression of GAD65 with SST, calretinin, NPY or calbindin in the Cx portion of D100 iCtrl or Mut Cx + GE fusion organoids revealed the presence of multiple interneuron subtypes **e,f**. Cell counting revealed trends for all comparisons and a statistically significant difference between iCtrl and Mut samples with respect to the percentage of cells expressing calretinin; $n=3$ fusion organoids per genotype, ≥ 980 cells for each sample counted, NS for all groups except calretinin. ANOVA $P=0.0003$, $F=4.665$, d.f. (between columns) = 7, followed by Sidak's correction for multiple comparisons between iCtrl and Mut samples for each marker; * $P=0.0391$ for iCtrl versus Mut calretinin; NS for all other comparisons. Plots in **d** and **f** display the full distribution of individual data points. Dashed and dotted lines indicate the median and quartile values, respectively.

Genes downregulated in Mut versus iCtrl (total cells) samples were also enriched for epilepsy risk (17% concordance), but not autism (Extended Data Fig. 5).

Genes that were upregulated in *MECP2*-mutant organoids were notably enriched for Gene Ontology (GO) terms associated with neuronal projection, morphogenesis and synaptic assembly, whereas genes that were downregulated were associated with mRNA catabolism, endoplasmic reticulum (ER) targeting and protein translation (Fig. 5a and Supplementary Table 3). Most of these changes, particularly those associated with synapses, were most prominent in the CFuPN and CPN clusters, but not

present in inhibitory neurons (Extended Data Fig. 7). Among the most upregulated genes in Mut organoids were known axonal and synapse-associated genes such as *PCLO*, *ROBO2*, *EFNB2* and *NRXN1* (Extended Data Figs. 5 and 6a and Supplementary Table 2). However, the most elevated gene in the absence of *MECP2* function within all clusters was *NNAT* (encoding neuronatin), which has been implicated in the control of ER stress, neuronal excitability, receptor trafficking and calcium-dependent signaling^{45,46}. *NNAT* was upregulated in all clusters but particularly high in the intermediate progenitor and inhibitory interneuron groups (Extended Data Fig. 6a).

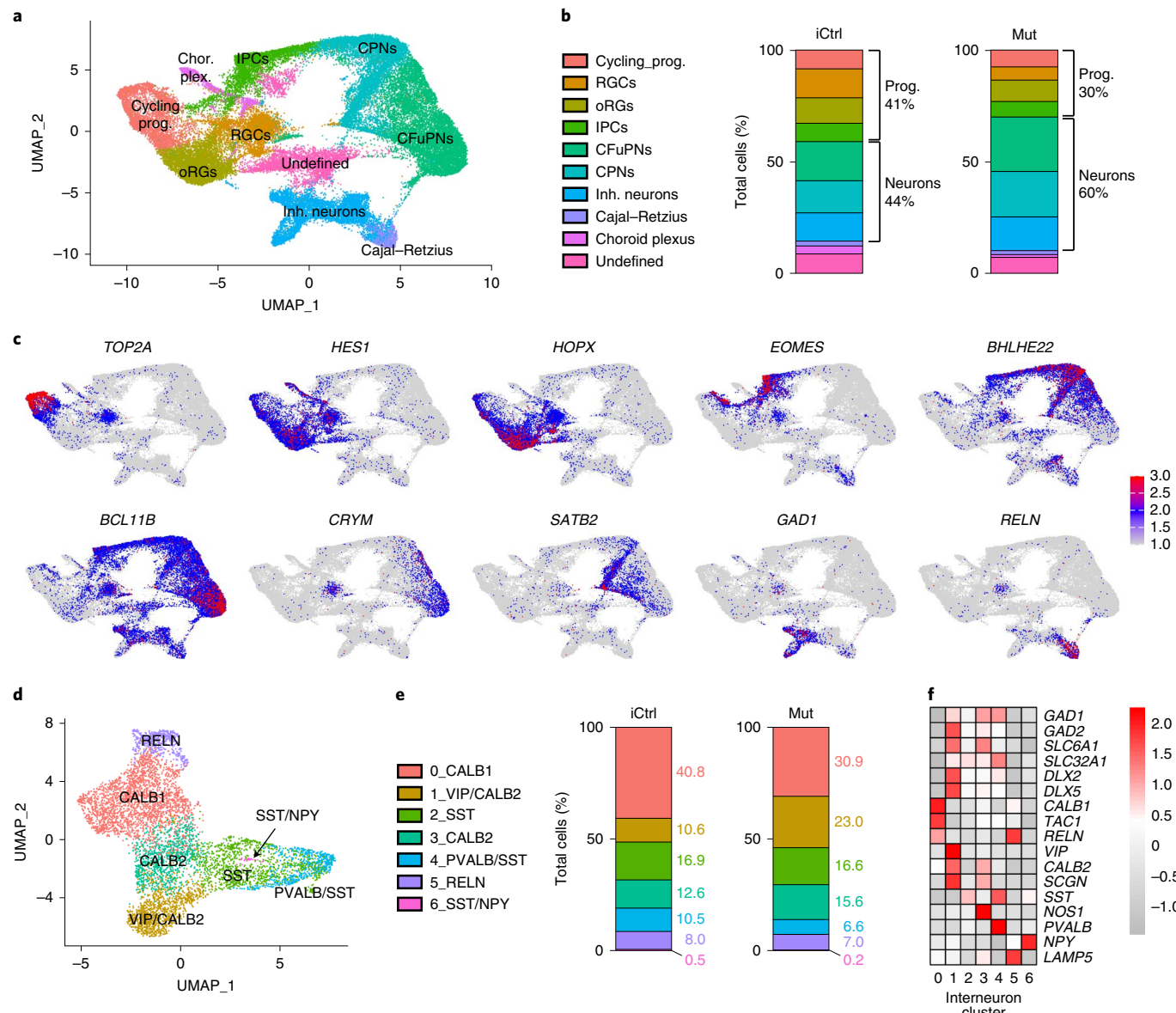


Fig. 4 | Single-cell transcriptomic analysis reveals the presence of diverse cellular populations in fusion organoids with a trend toward accelerated maturation and alterations in interneuron formation in MECP2-mutant samples. **a**, UMAP of combined iCtrl and Mut Cx and GE organoids. The plot includes cells from three D56 Cx and three GE organoids collected before fusion, three D70 Cx + GE fusion organoids, and three D100 Cx + GE fusion organoids. The total number of cells sequenced was: D56 iCtrl, 9,306; D56 Mut, 9,186; D70 iCtrl, 10,931; D70 Mut, 6,260; D100 iCtrl, 7,561; and D100 Mut, 6,698 cells. RGCs, radial glial cells; oRGs, outer radial glia cells. **b**, Plots display the mean percentage of cells in the fusion organoids representing each of the clusters in **a**. Separation of the data by iCtrl and Mut status showed a trend of reduced progenitors and more differentiated neurons in Mut organoids compared to iCtrl samples. **c**, UMAPs of key genes associated with each of the major clusters identified in **a**. **d**, Re-clustered UMAP of the interneuron subset from **a** with interneuron subtype markers identifying each re-clustered subset. **e**, Percentage of cells for each of the clusters in **d** segregated by iCtrl and Mut status revealed increased numbers of interneurons expressing PVALB/SST and CALB1 in iCtrl organoids and cells expressing VIP and CALB2 in Mut samples. **f**, Heat map displaying the relative expression of canonical interneuron-related genes within the re-clustered groups.

Because we used kainate to stimulate neural oscillations in the fusion organoids, we surveyed the expression of kainate receptors between iCtrl and Mut fusion samples. While the predominant receptor *GRIK5* and *GRIK1*, *GRIK2* and *GRIK4* were comparably expressed, we found a small upregulation of *GRIK3* selectively in the CFuPN cluster within Mut organoids (Extended Data Fig. 6b). The significance of this elevation is unclear but may further predispose the Mut organoids to network hyperexcitability.

We lastly examined the status of synapse formation in the cortical compartment of iCtrl and Mut Cx+GE fusion organoids using

VGLUT1 and PSD95 co-staining to distinguish presynaptic and postsynaptic components of excitatory synapses and VGAT and GEPHYRIN co-staining for inhibitory synapses. Consistent with the transcriptomic results, we found a significant increase in the density of excitatory puncta in Mut organoids compared to iCtrl samples, without any change in inhibitory synapses (Fig. 5b,c). Collectively, these results suggest that MECP2 deficiency results in changes in gene expression that ultimately alter the balance of excitatory versus inhibitory synapses and may thereby impact neuronal network functions.

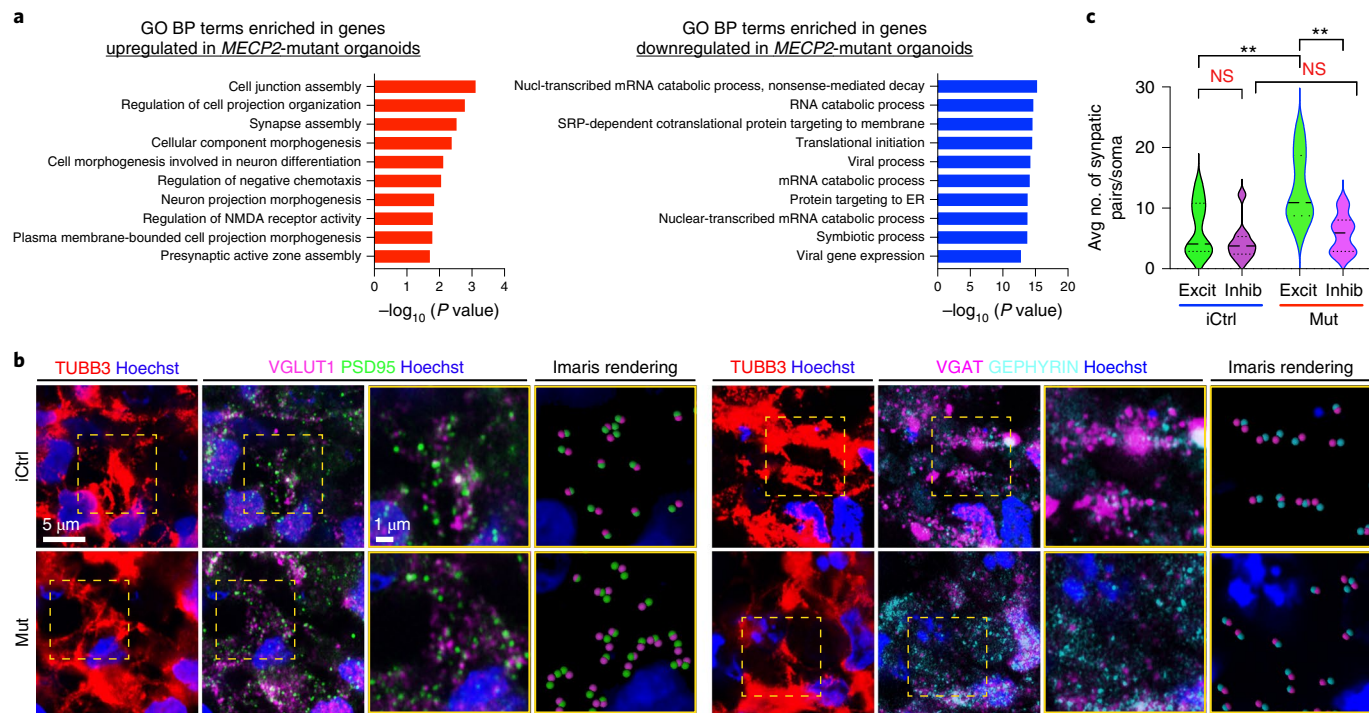


Fig. 5 | Gene Ontology and synaptic staining analyses reveal defects in the balance of excitatory and inhibitory synapses in *MECP2*-mutant fusion organoids. **a**, Top ten most enriched GO biological process (BP) terms associated with upregulated or downregulated differentially expressed genes when comparing Mut and iCtrl samples across all cells. **b**, Immunohistochemical analysis of excitatory (VGLUT1/PSD) and inhibitory (VGAT/GEPHYRIN) presynaptic and postsynaptic puncta revealed an increase in excitatory synapses in Mut Cx + GE fusion organoids. The yellow dashed boxes display representative TUBB3⁺ regions that were used for analyses. The adjacent two images demonstrate the raw immunohistochemical image followed by Imaris software renderings of the colocalized presynaptic and postsynaptic markers. The final two images are magnified versions of the boxed areas. **c**, Plots of the number of synapses per cell. Data were pooled from multiple organoids. VGLUT1/PSD95 (Excit), $n=3$ organoids for both iCtrl and Mut samples, 1,180 cells; VGAT/GEPHYRIN (Inhibit), $n=4$ organoids for iCtrl and Mut samples, 1,654 cells. ANOVA $P=0.0002$, $F=8.387$, d.f. (between columns)=3, followed by Tukey's multiple-comparisons test; ** $P=0.0088$ for Excit iCtrl versus Excit Mut; ** $P=0.0014$ for Excit Mut versus Inhib Mut. Plots display the full distribution of individual data points with dashed and dotted lines indicating the median and quartile values, respectively.

Hyperexcitability and hypersynchrony in *MECP2*-mutant organoids. Consistent with these synaptic data, and even more striking, were activity differences revealed through GCaMP6f imaging. Mut Cx + GE fusions exhibited epochs of spontaneously synchronized calcium transients (Fig. 6a–c and Supplementary Videos 8 and 9) reminiscent of the synchronizations observed following administration of GABA_A receptor antagonists to control samples (Fig. 2c–e and Supplementary Videos 4 and 5) and the epileptiform changes seen in murine Rett syndrome models⁴⁷. These results were notably consistent across the different batches of organoids tested and two independent Mut cell lines generated from the same individual with Rett syndrome (Extended Data Fig. 1b,d). Previous reports have indicated increased activity and diminished size of neural microcircuits in mouse chemoconvulsant epilepsy models⁴⁸. We similarly observed that increased synchronization of calcium transients in Mut Cx + GE organoids was accompanied by reductions in both the size of microcircuit clusters and the number of neurons within each cluster (Extended Data Fig. 8a).

To extend these results further, we generated Cx + GE fusion organoids from the second group of hiPSC lines from individuals with Rett syndrome (hereafter iCtrl-II and Mut-II; two independent lines of Mut-II were used). GCaMP6f imaging revealed decorrelated activity in iCtrl-II organoids reminiscent of the results from prior H9 hESC and iCtrl-I hiPSC Cx + GE experiments (Extended Data Fig. 4b versus Figs. 2c and 6a). By contrast, Mut-II organoids exhibited multiple instances of individual neurons firing at a rapid and persistent rate (Extended Data

Fig. 4b and Supplementary Videos 10 and 11), although we did not observe hypersynchronous bursts as seen in Mut-I organoids (Extended Data Fig. 4b,c versus Fig. 6a,b). The rapid GCaMP6f activity in Mut-II organoids resulted in a significant decrease in the mean and median inter-spike interval and, as was the case with Mut-I organoids, an increase in the proportion of multi-spiking neurons (Extended Data Fig. 4d). Consonant with the lack of visible hypersynchronicity, there was no effect on the amplitude of synchronized transients (Extended Data Fig. 4d). These results were consistent with respect to organoid batches and cell lines used within the iCtrl-II versus Mut-II groupings, yet strikingly different between genotypes (Extended Data Fig. 1b,c). Collectively, these data demonstrate a high degree of consistency in aspects of the neural network dysfunction phenotype in *MECP2* Mut organoids associated with hyperexcitability, but also demonstrate distinct characteristics based on their patient origins.

***MECP2*-mutant organoids exhibit aberrant neural oscillations.** LFP recordings of iCtrl-I Cx + GE fusions demonstrated infrequent spikes and sustained low-frequency and gamma oscillations with few epochs of higher-frequency oscillations (>100 Hz), much like the profile exhibited by H9 hESC-derived fusion organoids (Fig. 7a–e versus Fig. 2f–h). By contrast, Mut-I Cx + GE organoids lacked low-frequency and gamma oscillations (Fig. 7a–c; ‘Mut’) and instead exhibited recurring epileptiform-appearing spikes and high-frequency oscillations (HFOs, ~200–500 Hz; Fig. 7a–g and Extended Data Fig. 9). These findings concurred

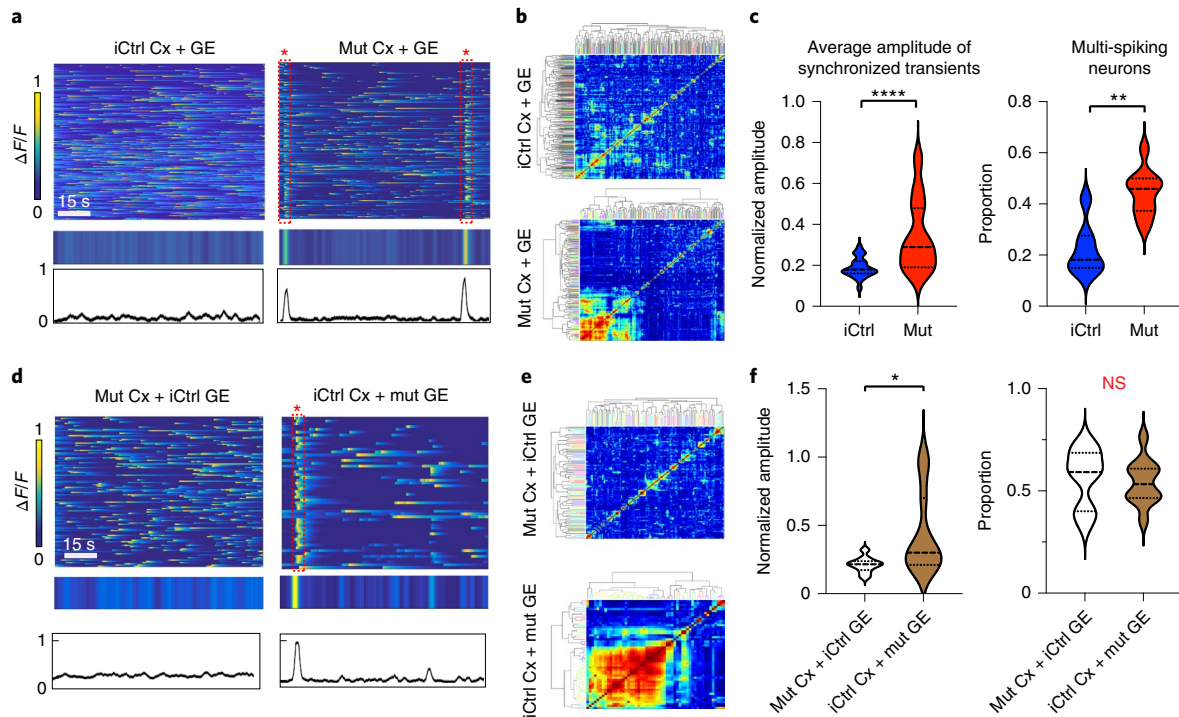


Fig. 6 | Rett syndrome fusion organoids display GE-dependent hypersynchronous neural network activity. **a**, Mut Cx + GE fusions exhibit spontaneous synchronized calcium transients that were not seen in iCtrl Cx + GE fusions, reflected in the raw $\Delta F/F$ colorized amplitude plot (top), synchronization amplitude plot (bottom) and clustergrams in **b**. **c**, Pooled data quantifications. $n=12$ independently generated iCtrl fusion organoids and $n=7$ independently generated Mut fusion organoids; *** $P<0.0001$ for the average amplitude of synchronized transients; ** $P=0.0012$ for multi-spiking neurons. Significance was assessed by two-sided Mann-Whitney U test. **d**, Mixed fusions with iCtrl Cx and Mut GE exhibited spontaneously synchronized calcium transients, whereas mixed fusions with Mut Cx and iCtrl GE did not, as seen in the raw $\Delta F/F$ colorized amplitude plot (top), synchronization amplitude plot (middle) and clustergrams in **e**. **f**, Pooled data quantifications. $n=10$ independently generated iCtrl Cx + Mut GE and $n=11$ Mut Cx + iCtrl GE fusion organoids; * $P=0.0308$, d.f.=19, $t=2.334$, two-tailed student's t -test. Plots in **c** and **f** display the full distribution of individual data points. Dashed and dotted lines indicate the median and quartile values, respectively.

with calcium indicator data showing rare but large high-amplitude calcium synchronizations or high-frequency firing in Mut fusion organoids that could result in spikes or HFOs, as opposed to the numerous small synchronizations seen in iCtrl samples, which likely generate sustained lower-frequency oscillations without epileptiform events (Fig. 6). Hypersynchrony, HFOs and spikes seen in Mut Cx + GE organoids are all consistent with the electrographic changes observed in human epilepsy^{49,50}. Indeed, electroencephalographic abnormalities and overt epilepsy were documented in patients with Rett syndrome whose hiPSCs were used in this study³⁹.

We also performed LFP recordings on Cx + GE organoids produced from iPSC lines from the second individual with Rett syndrome. iCtrl-II organoids displayed infrequent spikes and sustained low-frequency and gamma oscillations with few epochs of higher-frequency oscillations (>100 Hz) like iCtrl-I samples (Extended Data Figs. 10a–c ('iCtrl-II') versus Figs. 2f–h and 7a–e). By contrast, Mut-II Cx + GE organoids lacked low-frequency and gamma oscillations and instead exhibited recurring epileptiform-appearing spikes and HFOs (Extended Data Fig. 10a–c; 'Mut-II'). Quantification of these data revealed a significant loss of low gamma power in Mut-II as compared to iCtrl-II organoids, a modest reduction in high gamma power in Mut-II relative to iCtrl-II organoids and a substantial increase in spike frequency in Mut-II (Extended Data Figs. 10d,e). We again observed consistency in these measurements across organoid batches, independent cell lines from the same individual and within genotypes, with marked differences across genotypes (Extended Data Fig. 1b,d).

MECP2 deficiency in interneurons drives neural network dysfunction. Epilepsy is present in 60–80% of individuals with Rett syndrome and is thought to arise primarily from interneuron dysfunction^{51,52}, although *MECP2* loss in other cell types has also been implicated²². As our Cx and GE organoids are enriched in excitatory and inhibitory interneurons, respectively, we generated 'mixed' fusions in which either the Cx or the GE half of the fused structure was Mut-I, while the other half was iCtrl-I, as a means of determining the compartment and cell type in which MECP2 deficiency matters most. Mut-I Cx + iCtrl-I GE mixed-fusion organoids displayed calcium transients nearly identical to those in unmixed iCtrl Cx + GE fusions and did not show any evidence of hypersynchrony. By contrast, iCtrl-I Cx + Mut -I GE organoids exhibited hypersynchronous calcium transients like unmixed Mut-I Cx + GE fusions, although an increase in the proportion of multi-spiking neurons was not detected (Fig. 6d–f and Supplementary Videos 12 and 13).

We likewise found that Mut-I Cx + iCtrl-I GE organoids displayed an LFP profile nearly identical to unmixed iCtrl-I Cx + GE fusions (Fig. 7a–e and Extended Data Fig. 9). By contrast, iCtrl-I Cx + Mut-I GE organoids demonstrated frequent spikes and HFOs along with deficits in distinct lower-frequency oscillations and gamma activity, much like unmixed Mut-I Cx + GE fusions (Fig. 7a–e and Extended Data Fig. 9). Together, these data suggest that MECP2 deficiency in GE-derived interneurons is the primary driver of the neural network dysfunction within the fusion organoids.

Among these observations, changes in spike frequency and gamma oscillations may be of particular relevance as both human and murine *in vivo* studies have shown an inverse relationship

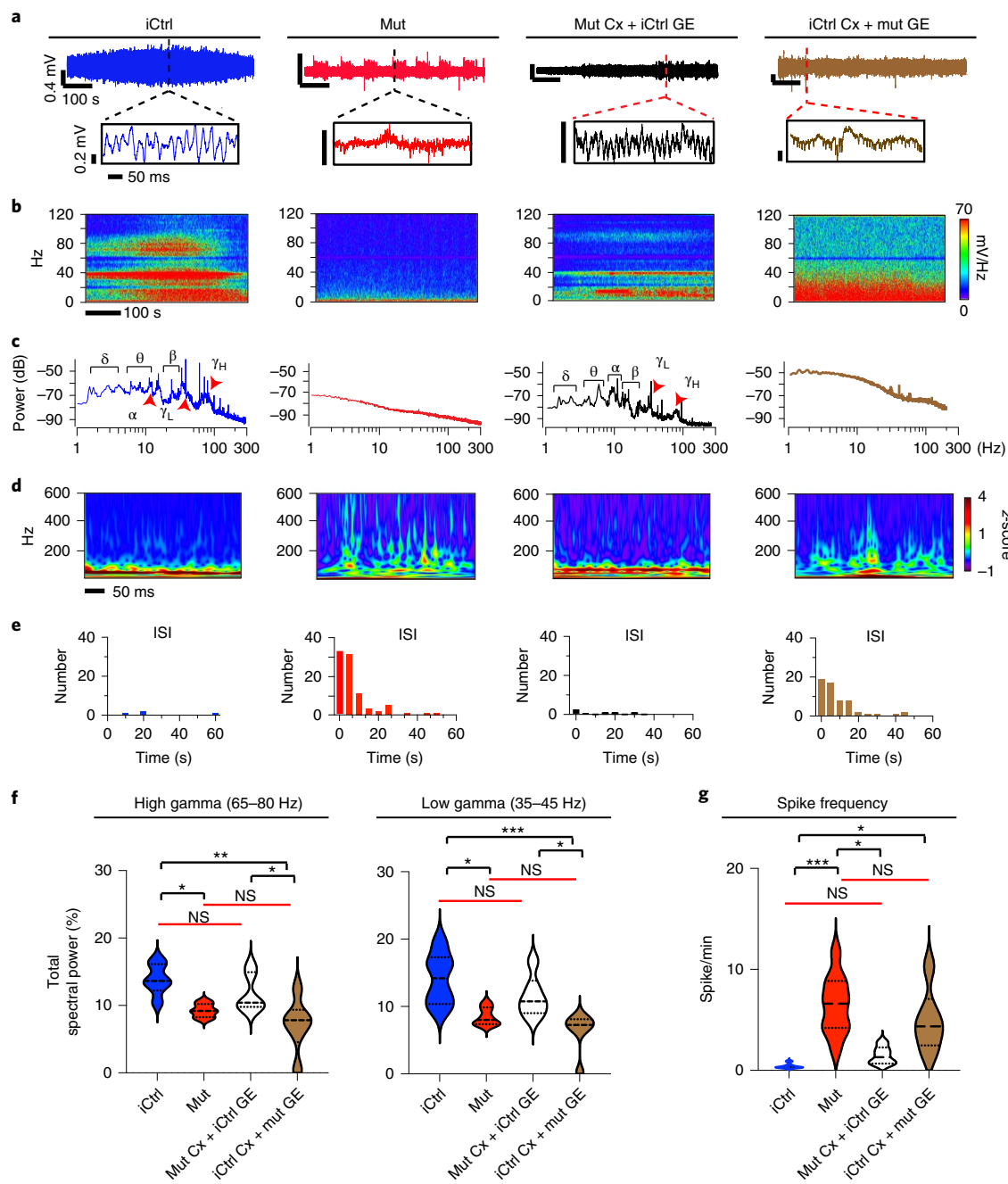


Fig. 7 | Rett syndrome fusion organoids display GE-dependent epileptiform changes. **a**, Raw trace of a representative 10-min LFP recording (top) and time-expanded window (bottom) from unmixed Mut or iCtrl Cx + GE fusion organoids and Mut/iCtrl mixed Cx + GE fusions. **b,c**, Spectrograms and periodograms derived from the entire recordings shown in **a**. **d**, Morlet plot showing high-frequency activity associated with the time-expanded segments shown in **a**. **e**, Frequency histogram of inter-spike intervals derived from the raw trace in **a**. **f**, Quantification of high gamma and low gamma spectral power from LFP recordings demonstrated a significant decrease in gamma power in Mut Cx + GE fusions and mixed fusions with a Mut GE. High gamma; ordinary ANOVA, overall $P=0.0020$, $F=7.089$, d.f. (between columns)=3, Tukey's multiple-comparisons test, ** $P=0.0018$, * $P=0.0353$ iCtrl versus Mut and * $P=0.0345$ Mut Cx + iCtrl GE versus iCtrl Cx + Mut GE. Low gamma; ordinary ANOVA, overall $P=0.0174$, $F=8.038$, d.f. (between columns)=3, Tukey's multiple-comparison test, *** $P=0.0009$, * $P=0.0174$ iCtrl versus Mut, * $P=0.0309$ Mut Cx + iCtrl GE versus iCtrl Cx + Mut GE. **g**, Spike frequency across multiple independent experiments, Kruskal-Wallis test, overall $P=0.0002$, Dunn's multiple-comparisons test, *** $P=0.002$, * $P=0.0159$ iCtrl versus iCtrl GE + Mut Cx and * $P=0.0416$ Mut versus Mut Cx + iCtrl GE. $n=6$ independently generated organoids for each condition (iCtrl and Mut) in **f** and **g**. Plots in **f** and **g** display the full distribution of individual data points. Dashed and dotted lines indicate the median and quartile values.

between gamma-band power and epileptiform discharges^{14,15}. In addition, gamma oscillations are thought to require complex inhibitory-excitatory network interactions that are highly prone to disruption by epileptic or interictal discharges¹⁴. Strong gamma peaks were consistently present in unmixed iCtrl-I Cx + GE

organoids and mixed Mut-I Cx + iCtrl GE organoids, and absent or reduced in amplitude in Mut-I Cx + GE and iCtrl-I Cx + Mut GE structures. Consistent with these conclusions, quantification of gamma spectral power revealed a comparable loss of both low and high gamma spectral power in the unmixed Mut-I organoids

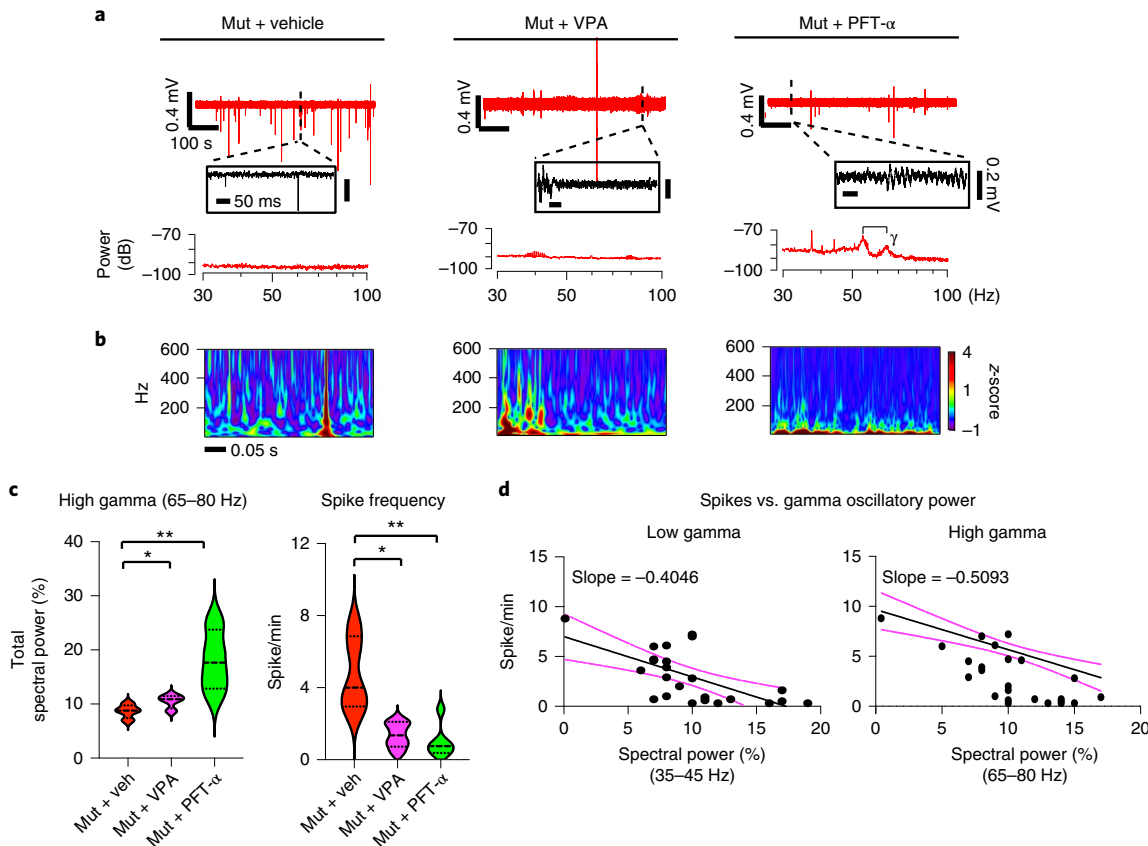


Fig. 8 | Partial restoration of gamma oscillations and suppression of HFOs in Rett syndrome fusion organoids with pifithrin- α . **a**, Raw trace (top), time-expanded window (middle) and periodogram (bottom) from representative Mut Cx + GE fusion organoids treated for 48 h with vehicle (dimethylsulfoxide; Veh), 2 mM VPA or 10 μ M pifithrin- α (PFT). **b**, Morlet plot was derived from the time-expanded segment in **a**. **c**, Quantification of high gamma oscillations and spike frequency in Mut Cx + GE showed a highly significant rescue of both high gamma spectral power and a reduction in spike frequency following treatment with PFT and a more modest rescue in both measures following VPA treatment. High gamma quantification; ordinary ANOVA, overall $P=0.0085$, $F=8.476$, d.f. (between columns)=2, Tukey's multiple-comparisons test, ** $P=0.0093$, * $P=0.0299$, $n=4$ independently generated organoids for each of the three conditions (Veh, VPA and PFT). Spike frequency following drug addition; Kruskal-Wallis test, overall $P=0.0020$, Dunn's multiple-comparisons test, ** $P=0.0042$, * $P=0.0420$. Plot displays the full distribution of individual data point. Dashed and dotted lines indicate the median and quartile values. **d**, Plots of high and low gamma spectral power versus spike frequency demonstrate an inverse relationship between gamma power and spiking. The solid black line is the best fit following simple linear regression, and the magenta lines indicate 95% confidence intervals for the estimated line of best fit. The slope of the line of best fit is indicated. The calculated slope is significantly different from zero with $P<0.0001$ for high gamma and $P=0.0007$ for low gamma.

and mixed iCtrl-I Cx + Mut GE organoids, as well as significantly increased spike frequency in these groups relative to unmixed iCtrl-I Cx + GE samples (Fig. 7f,g).

Neural oscillation defects can be restored by administration of pifithrin- α . A heralded, but largely unrealized, application of patient-derived hiPSCs is in personalized medicine. We therefore sought to determine the utility of the epileptiform phenotype observed in Rett syndrome organoids for drug testing. First, we used a broad-spectrum anti-seizure medication, sodium valproate (VPA), commonly used to treat epilepsy resulting from Rett Syndrome⁵³. We also tested a putative TP53 target inhibitor, pifithrin- α , based on previous studies showing that MECP2 deficiency leads to overactivation of the TP53 pathway and premature neuronal senescence^{39,54}. Consistent with its known spike suppressant properties, exposure to VPA for 48 h reduced spiking activity in the Mut-I Cx + GE organoids (Fig. 8a,c), although it did not reduce HFOs and had a modest effect on restoration of lower-frequency oscillations (Fig. 8a-c). Pifithrin- α similarly reduced spike frequency but remarkably also suppressed HFOs and resulted in the re-emergence of gamma oscillations

(Fig. 8a-c). A nearly identical response was also seen with Mut-II Cx + GE fusion organoids (Extended Data Fig. 10a-e). We combined all LFP experiments and plotted spike rate versus gamma spectral power for both low gamma and high gamma and observed the expected inverse relationship for cell lines from both individuals (Fig. 7f,g and Extended Data Fig. 10f). This inverse relationship is consistent with what has previously been described in both mouse models of neurological disease and patients with epilepsy^{14,15}.

To determine if drug effects were associated with changes in cell death, activating cleavage of caspase-3 was assessed by immunohistochemistry but did not reveal any discernable differences (Supplementary Fig. 4). We also did not observe any specific effects of pifithrin- α on iCtrl-I Cx + GE fusion LFP activity or cell death (Supplementary Fig. 5). Together, these results suggest that while VPA largely reduced neuronal hyperexcitability, pifithrin- α may additionally modulate more upstream excitatory-inhibitory physiological interactions resulting in a more global restoration of network-level functions. These findings further illustrate the potential value of the fusion organoid modeling approach in personalized drug discovery.

Discussion

Collectively, these experiments demonstrate the existence of highly sophisticated physiological activities within Cx+GE organoids, congruent with their cytoarchitectural and cellular complexity. These results stand in agreement with findings recently reported by Trujillo et al., who have also observed the emergence of neural oscillations in cortical organoids cultured for prolonged time periods using a different organoid protocol and recording approach¹¹. Our studies further demonstrate that the emergence of higher-order network activities such as multifrequency oscillations requires functional integration of inhibitory interneurons into the excitatory network framework as permitted by the organoid fusion technique, as no oscillations were apparent without them. Critically, this approach also allowed us to identify striking electrophysiological phenotypes in *MECP2*-mutant Cx+GE organoids despite their cytoarchitectural similarity to iCtrl samples. In addition, the use of hiPSCs derived from two individuals with Rett syndrome, each harboring unique *MECP2* mutations, allowed us to more confidently identify the physiological signatures of neural network dysfunction that arise in Rett syndrome brain organoids. There appeared to be a high degree of reproducibility and consistency in the results across multiple experiments, organoid batches, cell lines and modes of analysis, further confirming the validity of the fusion organoid model.

Although we did not observe overt differences between Mut and iCtrl fusion organoids by immunohistochemical analyses or scRNA-seq with respect to major cell types, we did see trends that may contribute to the marked physiological phenotypes we have documented. Perhaps most notably, and consistent with our finding that the interneuron-enriched GE compartment primarily accounts for the physiological changes in Mut fusion organoids, was a relative enrichment of PVALB interneurons in iCtrl and VIP interneurons in Mut samples. Together with SST interneurons, these two subtypes provide crucial inhibitory input to pyramidal (excitatory) cells that, in turn, mediate neural oscillations⁵⁵. Specifically, PVALB neuron activity is thought to mediate 20–80-Hz oscillations including gamma activity, whereas SST interneurons, which are directly inhibited by VIP, mediate oscillations in the 5–30-Hz frequency range^{55,56}. The consistent loss of lower-frequency oscillations in Mut fusion organoids may arise from VIP-mediated reductions in SST activity, whereas reductions in PVALB cells may contribute to the loss of gamma oscillations. Substantial reductions in PVALB⁺ interneurons have been seen in the prefrontal cortex of individuals with autism⁵⁷.

Of note, and consistent with our LFP findings, we also observed a relative decrease in SST expression in Mut organoids by immunohistochemistry, although this was not observed in our scRNA-seq data. We also saw an increase in excitatory but not inhibitory synaptic puncta in Mut organoids, likely related to the transcriptomic changes revealed by our scRNA-seq analysis. Genes that were differentially expressed in *MECP2*-mutant organoids showed strong associations with axonal growth, synapse formation, autism risk and epilepsy. The relative increase in excitatory input may further contribute to disruptions in neural oscillations and predispose the organoids toward hyperexcitability.

In addition to our mechanistic studies, we sought to exploit our system as a new platform for drug testing. We were intrigued to discover a more complete rescue of the Mut phenotype with a new drug, pifithrin- α , than was seen with a traditional anti-seizure medication, VPA. Pifithrin- α is a TP53 inhibitor shown previously to counteract cellular stress and senescence responses seen in *MECP2*-deficient neurons *in vitro*³⁹. These data merit future investigations into both the neuroregulatory actions of pifithrin- α as well as the role of *MECP2* in the repression of TP53-mediated senescence pathways.

In summary, these findings illustrate the potential of brain organoids both as a unique platform for characterizing human

neural networks and for personalized drug discovery and research. A remaining challenge is to delineate the precise microcircuit and cell-type-specific perturbations that underlie both the oscillatory and pathological epileptiform-like changes revealed in these studies. Important clues in the pursuit of this endeavor have already been revealed by the transcriptomic analyses that we have completed. The fusion organoid system that we used is highly amenable to such detailed cellular and circuit analyses and provides unprecedented opportunities for modeling neural network dysfunction associated with a variety of human neurological disorders.

Online content

Any methods, additional references, Nature Research reporting summaries, source data, extended data, supplementary information, acknowledgements, peer review information; details of author contributions and competing interests; and statements of data and code availability are available at <https://doi.org/10.1038/s41593-021-00906-5>.

Received: 29 August 2019; Accepted: 8 July 2021;

Published online: 23 August 2021

References

1. Di Lullo, E. & Kriegstein, A. R. The use of brain organoids to investigate neural development and disease. *Nat. Rev. Neurosci.* **18**, 573–584 (2017).
2. Amin, N. D. & Pasca, S. P. Building models of brain disorders with three-dimensional organoids. *Neuron* **100**, 389–405 (2018).
3. Qian, X., Song, H. & Ming, G. L. Brain organoids: advances, applications and challenges. *Development* **146**, dev166074 (2019).
4. Rakic, P. Evolution of the neocortex: a perspective from developmental biology. *Nat. Rev. Neurosci.* **10**, 724–735 (2009).
5. Molnar, Z. et al. Evolution and development of the mammalian cerebral cortex. *Brain Behav. Evol.* **83**, 126–139 (2014).
6. van der Worp, H. B. et al. Can animal models of disease reliably inform human studies? *PLoS Med.* **7**, e1000245 (2010).
7. Dawson, T. M., Golde, T. E. & Lagier-Tourenne, C. Animal models of neurodegenerative diseases. *Nat. Neurosci.* **21**, 1370–1379 (2018).
8. Stam, C. J. Modern network science of neurological disorders. *Nat. Rev. Neurosci.* **15**, 683–695 (2014).
9. Palop, J. J. & Mucke, L. Network abnormalities and interneuron dysfunction in Alzheimer disease. *Nat. Rev. Neurosci.* **17**, 777–792 (2016).
10. Sun, A. X. et al. Potassium channel dysfunction in human neuronal models of Angelman syndrome. *Science* **366**, 1486–1492 (2019).
11. Trujillo, C. A. et al. Complex oscillatory waves emerging from cortical organoids model early human brain network development. *Cell Stem Cell* **25**, 558–569 (2019).
12. Buzsaki, G. & Wang, X. J. Mechanisms of gamma oscillations. *Annu Rev. Neurosci.* **35**, 203–225 (2012).
13. Headley, D. B. & Paré, D. Common oscillatory mechanisms across multiple memory systems. *NPJ Sci. Learn.* **2**, 1 (2017).
14. Verret, L. et al. Inhibitory interneuron deficit links altered network activity and cognitive dysfunction in Alzheimer model. *Cell* **149**, 708–721 (2012).
15. Matsumoto, J. Y. et al. Network oscillations modulate interictal epileptiform spike rate during human memory. *Brain* **136**, 2444–2456 (2013).
16. van Dellen, E. et al. Local polymorphic delta activity in cortical lesions causes global decreases in functional connectivity. *Neuroimage* **83**, 524–532 (2013).
17. Watanabe, M. et al. Self-organized cerebral organoids with human-specific features predict effective drugs to combat Zika virus infection. *Cell Rep.* **21**, 517–532 (2017).
18. Bagley, J. A., Reumann, D., Bian, S., Levi-Strauss, J. & Knoblich, J. A. Fused cerebral organoids model interactions between brain regions. *Nat. Methods* **14**, 743–751 (2017).
19. Birey, F. et al. Assembly of functionally integrated human forebrain spheroids. *Nature* **545**, 54–59 (2017).
20. Xiang, Y. et al. Fusion of regionally specified hPSC-derived organoids models human brain development and interneuron migration. *Cell Stem Cell* **21**, 383–398 (2017).
21. Sakaguchi, H., et al. Self-organized synchronous calcium transients in a cultured human neural network derived from cerebral organoids. *Stem Cell Reports* **13**, 458–473 (2019).
22. Lyst, M. J. & Bird, A. Rett syndrome: a complex disorder with simple roots. *Nat. Rev. Genet.* **16**, 261–275 (2015).
23. Garofalo, E. A., Drury, I. & Goldstein, G. W. EEG abnormalities aid diagnosis of Rett syndrome. *Pediatr. Neurol.* **4**, 350–353 (1988).

24. Operto, F. F., Mazza, R., Pastorino, G. M. G., Verrotti, A. & Coppola, G. Epilepsy and genetic in Rett syndrome: a review. *Brain Behav.* **9**, e01250 (2019).
25. Watanabe, M., et al. TGF β superfamily signaling regulates the state of human stem cell pluripotency and competency to create telencephalic organoids. Preprint at *bioRxiv*, <https://doi.org/10.1101/2019.12.13.875773> (2019).
26. Hendry, S. H., Schwark, H. D., Jones, E. G. & Yan, J. Numbers and proportions of GABA-immunoreactive neurons in different areas of monkey cerebral cortex. *J. Neurosci.* **7**, 1503–1519 (1987).
27. Sahara, S., Yanagawa, Y., O’Leary, D. D. & Stevens, C. F. The fraction of cortical GABAergic neurons is constant from near the start of cortical neurogenesis to adulthood. *J. Neurosci.* **32**, 4755–4761 (2012).
28. Ferando, I. & Mody, I. In vitro gamma oscillations following partial and complete ablation of delta subunit-containing GABA_A receptors from parvalbumin interneurons. *Neuropharmacology* **88**, 91–98 (2015).
29. Pnevmatikakis, E. A., et al. Simultaneous denoising, deconvolution and demixing of calcium imaging data. *Neuron* **89**, 285–299 (2016).
30. Zhou, P., et al. Efficient and accurate extraction of in vivo calcium signals from microendoscopic video data. *Elife* **7**, e28728 (2018).
31. Buzsaki, G. & Draguhn, A. Neuronal oscillations in cortical networks. *Science* **304**, 1926–1929 (2004).
32. Wang, D. D. & Kriegstein, A. R. GABA regulates excitatory synapse formation in the neocortex via NMDA receptor activation. *J. Neurosci.* **28**, 5547–5558 (2008).
33. Wang, D. D. & Kriegstein, A. R. Blocking early GABA depolarization with bumetanide results in permanent alterations in cortical circuits and sensorimotor gating deficits. *Cereb. Cortex* **21**, 574–587 (2011).
34. Leonard, H., Cobb, S. & Downs, J. Clinical and biological progress over 50 years in Rett syndrome. *Nat. Rev. Neurol.* **13**, 37–51 (2017).
35. Mellios, N., et al. MeCP2-regulated miRNAs control early human neurogenesis through differential effects on ERK and AKT signaling. *Mol. Psychiatry* **23**, 1051–1065 (2018).
36. Armstrong, D. D., Dunn, K. & Antalffy, B. Decreased dendritic branching in frontal, motor and limbic cortex in Rett syndrome compared with trisomy 21. *J. Neuropathol. Exp. Neurol.* **57**, 1013–1017 (1998).
37. Belichenko, P. V., et al. Widespread changes in dendritic and axonal morphology in *Mecp2*-mutant mouse models of Rett syndrome: evidence for disruption of neuronal networks. *J. Comp. Neurol.* **514**, 240–258 (2009).
38. Marchetto, M. C., et al. A model for neural development and treatment of Rett syndrome using human induced pluripotent stem cells. *Cell* **143**, 527–539 (2010).
39. Ohashi, M., et al. Loss of MECP2 leads to activation of P53 and neuronal senescence. *Stem Cell Reports* **10**, 1453–1463 (2018).
40. D’Haene, E., et al. A neuronal enhancer network upstream of MEF2C is compromised in patients with Rett-like characteristics. *Hum. Mol. Genet.* **28**, 818–827 (2019).
41. Wang, J., et al. Novel *MEF2C* point mutations in Chinese patients with Rett (like) syndrome or non-syndromic intellectual disability: insights into genotype-phenotype correlation. *BMC Med. Genet.* **19**, 191 (2018).
42. Salpietro, V., et al. AMPA receptor GluA2 subunit defects are a cause of neurodevelopmental disorders. *Nat. Commun.* **10**, 3094 (2019).
43. Huisman, S., et al. Phenotypes and genotypes in individuals with *SMC1A* variants. *Am. J. Med. Genet. A* **173**, 2108–2125 (2017).
44. Lopes, F., et al. Identification of novel genetic causes of Rett syndrome-like phenotypes. *J. Med. Genet.* **53**, 190–199 (2016).
45. Oyang, E. L., Davidson, B. C., Lee, W. & Poon, M. M. Functional characterization of the dendritically localized mRNA neuronatin in hippocampal neurons. *PLoS ONE* **6**, e24879 (2011).
46. Sharma, J., et al. Neuronatin-mediated aberrant calcium signaling and endoplasmic reticulum stress underlie neuropathology in Lafora disease. *J. Biol. Chem.* **288**, 9482–9490 (2013).
47. Lu, H., et al. Loss and gain of MeCP2 cause similar hippocampal circuit dysfunction that is rescued by deep brain stimulation in a Rett syndrome mouse model. *Neuron* **91**, 739–747 (2016).
48. Feldt Muldoon, S., Soltesz, I. & Cossart, R. Spatially clustered neuronal assemblies comprise the microstructure of synchrony in chronically epileptic networks. *Proc. Natl Acad. Sci. USA* **110**, 3567–3572 (2013).
49. Bragin, A., Engel, J. Jr., Wilson, C. L., Fried, I. & Buzsaki, G. High-frequency oscillations in human brain. *Hippocampus* **9**, 137–142 (1999).
50. Bragin, A., Wilson, C. L., Almajano, J., Mody, I. & Engel, J. Jr. High-frequency oscillations after status epilepticus: epileptogenesis and seizure genesis. *Epilepsia* **45**, 1017–1023 (2004).
51. Ito-Ishida, A., Ure, K., Chen, H., Swann, J. W. & Zoghbi, H. Y. Loss of MeCP2 in parvalbumin-and somatostatin-expressing neurons in mice leads to distinct Rett syndrome-like phenotypes. *Neuron* **88**, 651–658 (2015).
52. Krajnc, N. Management of epilepsy in patients with Rett syndrome: perspectives and considerations. *Ther. Clin. Risk Manag.* **11**, 925–932 (2015).
53. Vignoli, A., et al. Effectiveness and tolerability of antiepileptic drugs in 104 girls with Rett syndrome. *Epilepsy Behav.* **66**, 27–33 (2017).
54. Squillaro, T., et al. Reduced expression of MECP2 affects cell commitment and maintenance in neurons by triggering senescence: new perspective for Rett syndrome. *Mol. Biol. Cell* **23**, 1435–1445 (2012).
55. Lee, B., Shin, D., Gross, S. P. & Cho, K. H. Combined positive and negative feedback allows modulation of neuronal oscillation frequency during sensory processing. *Cell Rep.* **25**, 1548–1560 (2018).
56. Chen, G., et al. Distinct inhibitory circuits orchestrate cortical beta and gamma band oscillations. *Neuron* **96**, 1403–1418 (2017).
57. Hashemi, E., Ariza, J., Rogers, H., Noctor, S. C. & Martinez-Cerdeno, V. The number of parvalbumin-expressing interneurons is decreased in the prefrontal cortex in autism. *Cereb. Cortex* **27**, 1931–1943 (2017).

Publisher’s note Springer Nature remains neutral with regard to jurisdictional claims in published maps and institutional affiliations.

© The Author(s), under exclusive licence to Springer Nature America, Inc. 2021

Methods

hESC and hiPSC culture and organoid generation. All hiPSC experiments were conducted following prior approval from the University of California, Los Angeles (UCLA) Embryonic Stem Cell Research Oversight (ESCRO) committee and Institutional Review Board. Cx and GE organoids were generated from the H9 hESC line³⁸ or Rett hiPSCs³⁹ as described previously¹⁷ and outlined in schematic form in Fig. 1a. Fusion was performed with minor modifications as previously reported¹⁹. Cx and GE organoids were cut at D56 and two halves (for example, Cx+GE or Cx+Cx) were combined in a microcentrifuge tube containing 300 µl of N2B27 medium¹⁷ and placed in a hyperoxic incubator containing 5% CO₂ and 40% O₂ for 72 h. Fused structures were then carefully transferred to 24-well oxygen-permeable dishes (Lumox, Sarstedt) and maintained in a hyperoxic environment with media changes every other day until their use. Neuron migration experiments were conducted by infection of either a Cx or GE organoid with 5 µl of ~1.98 × 10¹³ ml⁻¹ AAV1-tdTomato (pENN.AAV.CAG.tdTomato.WPRE.SV40, a gift of J. M. Wilson, University of Pennsylvania Vector Core AV-1-PV3365) on D56, and fusion was performed as described 3 d after infection.

Generation of Rett hiPSCs. Rett iPSCs were derived from fibroblast lines GM07982 and GM17567 obtained from the National Institute of General Medical Sciences Cell Repository maintained at the Coriell Institute for Medical Research, and generated by lentiviral transduction of the cells with the Yamanaka factors (Oct4, Klf4, Sox2 and cMyc) as previously described³⁹. GM07982 cells were isolated from a 25-year-old female noted to have electroencephalographic abnormalities, and found to contain a frameshift mutation, 705delG, in the *MECP2* gene resulting in a premature stop codon and protein truncation (E235fs). GM17567 cells were isolated from a 5-year-old female with a history of abnormal electroencephalograms and seizures and found to harbor an A>G missense mutation at nucleotide 1461 (c.1461A>G), resulting in a substitution of a tryptophan in place of the stop codon at codon 487 (p.Ter487Trp). As females with Rett syndrome are typically heterozygous for the *MECP2* mutation, the collected fibroblasts are mosaic in their *MECP2* protein status with approximately half of the cells expressing the nonmutant allele. Unlike murine cells, the inactive X chromosome in human cells remains inactive after reprogramming to pluripotency³⁹, allowing the generation *MECP2*-mutant and iCtrl hiPSCs from the same patient fibroblasts. Confirmation of *MECP2* control or mutant status was achieved through immunostaining and immunoblotting analyses of the iPSC lines and differentiated organoids.

Immunohistochemistry. Organoids were immersion fixed in 4% paraformaldehyde, cryoprotected in 30% sucrose, frozen in Tissue-Tek Optimal Cutting Temperature medium (Sakura) and cryosectioned. Immunostaining was performed using previously published laboratory protocols^{17,60}. Primary antibodies used included the following: goat anti-BRN2 (POU3F2; Santa Cruz Biotechnology, sc-6029), 1:4,000 dilution; mouse anti-CALBINDIN (clone CB-955, Sigma-Aldrich, C9848), 1:5,000 dilution; rabbit anti-CALRETININ (EMD Millipore, AB5054), 1:2,000 dilution; rabbit anti-cleaved CASPASE-3 (Asp175; Cell Signaling, 9661), 1:500 dilution; rat anti-CTIP2 (BCL11B; Abcam, ab18465), 1:1,000 dilution; rabbit anti-DLX1 (ref.⁶¹; generous gift of S. K. Lee and J. Lee), 1:3,000 dilution; guinea pig anti-DLX2 (ref.⁶²; generous gift of K. Yoshikawa and H. Shinagawa), 1:3,000 dilution; guinea pig anti-DLX5 (ref.⁶²; generous gift of K. Yoshikawa and H. Shinagawa), 1:3,000 dilution; rabbit anti-FOXP1 (Abcam, ab18259), 1:1,000 dilution; rabbit anti-GABA (Sigma-Aldrich, A2052), 1:10,000 dilution; mouse anti-GAD65 (BD Biosciences, 559931), 1:200 dilution; mouse anti-GEPRYRIN (Synaptic Systems, 147021), 1:500 dilution; goat anti-LHX2 (C-20, Santa Cruz Biotechnology, sc-19344), 1:1,000 dilution; rabbit anti-MECP2 (Diagenode, C15410052), 1:1,000 dilution; mouse anti-N-CADHERIN (CDH2, BD Biosciences, 610920), 1:800 dilution; rabbit anti-NPY (EMD Millipore, AB10980), 1:1,000 dilution; mouse anti-NKX2.1 (Novocastra NCL-L-TTR-1), 1:500 dilution; mouse anti-PAX6 (Developmental Studies Hybridoma Bank), 1:100 dilution; rabbit anti-PAX6 (MBL International, PD022), 1:1,000 dilution; mouse anti-PSD95 (Millipore, MAB1598), 1:1,000 dilution; mouse anti-SATB2 (Abcam, ab51502), 1:100 dilution; goat anti-SOX2 (Santa Cruz Biotechnology, sc-17320) 1:100 dilution; rat anti-SST (EMD Millipore MAB354), 1:100 dilution; rabbit anti-TBR1 (Abcam, ab31940), 1:2,000 dilution; chicken anti-TBR2 (EOMES; EMD Millipore, AB15894), 1:1,000 dilution; rabbit anti-TUBULIN B3 (TUBB3, BioLegend, 802001), 1:1,000 dilution; guinea pig anti-VGAT (Synaptic Systems, 131004), 1:1,000 dilution; guinea pig anti-VGLUT1 (SLC17A7; EMD Millipore AB5905), 1:1,000 dilution. Secondary antibody staining was conducted using Dylight 405-, FITC-, Alexa 488-, Cy3-, Alexa 594-, Cy5-, Alexa 647- and Dylight 647-conjugated donkey anti-species-specific IgG or IgM antibodies (Jackson ImmunoResearch or Invitrogen/Molecular Probes) at a 1:1,000 dilution. Nuclei were often counterstained using Hoechst 33258 added to the secondary antibody mix at a final concentration of 1 µg ml⁻¹. Single-plane and tiled composite images were obtained using a ×10 or ×20 objective on a Zeiss LSM 800 (running Zen 2.3 Blue edition software) or LSM 700 (running Zen 2011 Black edition software) confocal microscope, except for synaptic puncta, which were imaged using a ×63 objective on a Zeiss LSM 880 confocal microscope equipped with Airyscan technology (running Zen 2.3 Black edition software). All images that were directly compared

were obtained with identical laser power settings. Image adjustments were limited to brightness, contrast and level and were applied equally to all images in a set being compared. ImageJ/Fiji (versions 1 and 2 (ref.⁶³) and Adobe Photoshop (2019, 2020 and 2021) software was used for image adjustments. Composite figures were assembled using Adobe Illustrator (2019, 2020 and 2021).

Sample preparation for single-cell sequencing. Papain dissociation reagents were prepared according to the manufacturer's recommendations for the Papain Dissociation System (Worthington, LK003150), with a slight modification. Papain was resuspended in 5 ml Hibernate E medium (BrainBits, HE) containing N2 and B27 supplements (Life Technologies, 17502048 and 12587010; HNB) to yield a final concentration of 20 U papain per ml, to negate the need for 95% O₂/5% CO₂ equilibration. DNase was resuspended in EBSS as recommended and mixed gently to avoid shearing before being added to the papain solution. The final papain/DNase solution was then incubated at 37°C for 10 min before use to ensure complete solubilization. Three unfused Cx and GE (for D56) or three fused organoids (for D70 and D100) were combined into a single tube for each dissociation. To dissociate, organoids were washed twice with PBS (Fisher Scientific, SH3002802) in a 1.5-ml microcentrifuge tube before being transferred to a 10-cm dish containing fresh PBS. Organoids were gently diced into small chunks using a single-edge razor blade (Fisher Scientific, 12-640), and then transferred to a 15-ml conical tube and pelleted to remove the PBS. Organoid chunks were subsequently resuspended in 2 ml of papain/DNase solution at a final concentration of 20 U ml⁻¹. Organoids were incubated at 37°C with constant agitation for 30 min. After 30 min, the organoids were manually triturated five times using a 5-ml pipette to break up clumps, then placed at 37°C for a further 15 min. After 15 min, organoids were very gently titrated ten times with a P1000 tip and placed for a further 15 min at 37°C. In total, organoids were incubated in papain for 1 h to obtain a single-cell solution. The suspension was then filtered through a 40-µm strainer (Fisher Scientific, 08-771-1) into a fresh 15-ml conical tube and centrifuged at 300g for 10 min. The papain/DNase solution was removed and cells were resuspended in HNB lacking papain/DNase and centrifuged again. This process was repeated once more to completely remove papain and most cell debris. Finally, cells were resuspended in 1 ml of PBS containing 0.04% BSA and counted using Trypan blue staining and a Countess II Automated Cell Counter (Thermo Fisher, AMQAX1000). The resultant cell solution used for scRNA-seq contained >90% live cells and was adjusted to a cell concentration of 1,000 cells per µl before loading onto the 10X Genomics chip.

Single-cell RNA-seq data processing. FASTQ files for each sample were processed using the Cell Ranger 4.0.0 pipeline, and counts were generated with the 'cellranger count' function with the provided annotation refdata-gex-GRCh38-2020-A (10X Genomics). The data were combined into a Seurat object containing the six samples using Seurat (v3.2.0)^{64,65}. The data were filtered for cells with nFeatures_RNA > 500, nFeatures_RNA < mean+3*(standard deviation) and the percentage of mitochondrial genes < 10%. Data integration and batch correction were performed using the R package Linked Inference of Genomic Experimental Relationships (LIGER)⁶⁶. The data were normalized with the default parameters using Seurat functions NormalizeData() and FindVariableFeatures(). Data were then scaled using ScaleData(datExpr, split.by = 'orig.ident', do.center = FALSE). Next, data integration and batch correction were performed with the Seurat-wrapper functions for LIGER including RunOptimizeALS (datExpr, k = 20, lambda = 5, split.by = 'orig.ident') and RunQuantileNorm (datExpr, split.by = 'orig.ident') were performed. The data were then clustered using FindNeighbors (datExpr, reduction = 'iNMF', dims = 1:20) and FindClusters (datExpr, resolution = 0.3). tSNE visualization was performed using RunUMAP (datExpr, dims = 1:ncol(datExpr[[iNMF]])), reduction = 'iNMF'). Cluster marker genes were determined using differential expression between each cluster and the other clusters using the function FindAllMarkers (object = datExpr). Cluster assignments were manually performed referencing the calculated marker genes and common cell-type marker genes from literature sources^{67–72}. To estimate the uncertainty in cluster assignments, bootstrapped confidence intervals for cell-type proportions were generated using the R package single-cell differential composition with the function scDC_noClustering (cellTypes, subject, calCI = TRUE, calCI_method = 'percentile'), where 'cellTypes' were the cluster assignments and 'subject' was the cell genotypes⁷³. Differential expression between Mut and iCtrl samples overall and within each cluster was determined using FindMarkers (datExpr, ident.1 = 'Cluster#_Rett', ident.2 = 'Cluster#_Ctrl') and then filtered for genes with a false discovery rate < 0.05. Upregulated and downregulated genes that passed false discovery rate correction were ordered by fold change, and GO enrichment analysis was performed using the goset() function in gprofiler2_0.2.0 with the following parameters: Background genes were restricted to genes expressed in the dataset using custom_bg = background_genes, organism = 'hsapiens', ordered_query = TRUE, user_threshold = 0.05, correction_method = 'bonferroni' and sources = c('GO:BP','GO:MF','GO:CC','HP')^{74,75}. For representative GO plots (for example, Fig. 5a and Extended Data Fig. 7), term size was restricted to 1,000 and the top ten terms by -log₁₀(P value) were plotted with exclusion of successive terms containing identical evidence codes. For gene-list enrichment shown in Extended Data Fig. 5, the autism spectrum disorder-associated gene list was

downloaded from <https://gene.sfari.org/database/human-gene/> and Epilepsy list (C0014544) from <https://www.disgenet.org/search>. The gene lists were reduced to genes expressed in the single-cell organoid dataset and compared for overlap with the upregulated and downregulated genes between Mut and iCtrl samples when comparing all cells. To test for enrichment, Fisher's exact test was performed using the function 'fisher.test()' and then the corresponding *P* values were adjusted for multiple comparisons using p.adjust(*p*, method = 'bonferroni', *n* = length(*p*)).

Cell and synaptic puncta quantification. All cell quantifications were obtained using at least nine images per sample consisting of three noncontiguous regions per image and at least three images obtained from independent experiments. For GAD65 quantification, tiled images of fusion or unfused organoids were visualized in Photoshop (Adobe), a box of equal size was used to demarcate regions of interest on the outer edges of organoids, and total numbers of GAD65⁺ cells and Hoechst⁺ nuclei within the boxed region were manually tabulated. Synaptic puncta were identified and colocalized using Bitplane Imaris version 9.3 or 9.5 image processing software using the 'spots' identifier, set to detect identically sized objects surrounding TUBB3⁺ cellular processes and thresholded against Hoechst staining to exclude any nuclear overlap. The native 'colocalization' function on Imaris was used to identify overlapping puncta.

Live organoid calcium imaging. The genetically encoded calcium indicator GCaMP6f was introduced into organoids between D88–95 via infection with 5 μ l of 1.98×10^{13} GC ml⁻¹ pAAV1.Syn.GCaMP6f.WPRE.SV40 virus⁷⁶, a gift from D. Kim and the GENIE Project (Addgene viral preparation no. 100837-AAV1 or UPENN Vector core AV-1-PV2822). All imaging was performed 12–14 d after infection using a Scientifica two-photon microscope with a Coherent Chameleon tunable laser. Calcium transients were recorded at an excitation of 920 nm using a $\times 20$ 0.8-NA water-immersion objective (Nikon) and at a frame rate of 31 Hz with 512 \times 512-pixel resolution and 0.5 \times 0.5-mm field of view. Recording was performed in artificial cerebrospinal fluid (aCSF) as described below with additional 10 mM HEPES to maintain a pH of 7.3–7.4 in the absence of O₂/CO₂ perfusion (see 'Extracellular Recordings' below for details). Following initial imaging in the absence of drugs, organoids were then subjected to a 1-min incubation with the GABA_A receptor antagonist gabazine (25 μ M) or BMI (100 μ M), and the identical fields were reimaged after drug exposure.

Microcircuit identification. Raw Ca²⁺ imaging files in tiff format were processed to identify fluorescence transients ($\Delta F/F_0$) and spike estimation in MATLAB (MathWorks) using the CNMF-E methodology^{29,30}. Following CNMF-E-based data extraction neuronal microcircuit clusters were identified by performing hierarchical clustering on the correlation matrix of neuronal Ca²⁺ spiking data and analyzed based on work by Muldoon et al.⁴⁸. The correlation between all pairwise combinations of the time course of spikes for all neurons identified by CNMF-E was calculated to generate a correlation matrix. Following generation of the correlation matrix, linkage analysis was performed using the MATLAB 'linkage' function from the statistics toolbox (with 'complete'/furthest distance). The generated hierarchical clustering was input into the 'dendrogram' function from the MATLAB statistics toolbox with 'Color Threshold' fixed at 1.5 for all experimental groups. By then assigning each neuron to a cluster determined by its assigned color in the dendrogram, clusters were created in which there was high correlation between all neurons in the cluster. To calculate the number of pairs of neurons that were significantly correlated within each dataset, we first generated 1,000 shuffled time courses for each neuron using MATLAB's 'randperm' function. Pairwise correlations for the randomly shuffled time courses were calculated in the same way as the original data, and a pair of neurons were considered correlated if their correlation coefficient in the original data was significantly different to the 1,000 shuffled datasets with *P* < 0.05. To determine the threshold of simultaneous firing, the synchronization of the time-shuffled data was calculated, and the threshold was set at the 99th percentile of synchronization in the shuffled data. Synchronization above this threshold was considered 'synchronized'. These data were then plotted on a normalized y axis ranging from 0 (no synchronizations) to 1 (100% synchronization) and time on the x axis. The total number of synchronizations, average synchronization amplitude and average synchronization duration were then tabulated.

Extracellular recordings. Organoids were recorded between ~D100–107. Live organoids were perfused with 500 nM kainic acid in aCSF (containing 126 mM NaCl, 10 mM D-glucose, 1.2 mM MgCl₂, 2 mM CaCl₂, 5 mM KCl, 1.25 mM NaH₂PO₄, 1.5 mM sodium pyruvate, 1 mM L-glutamine and 26 mM NaHCO₃, pH 7.3–7.4, when bubbled with 95% O₂ and 5% CO₂) to initiate oscillatory network activity. LFP activity was recorded using a patch pipette filled with aCSF connected with a head stage to a field amplifier (A-M Systems, 3000) and bandpass filtered between 0.1 and 1,000 Hz to an instrumentation amplifier (Brownlee BP Precision, 210A). Field potentials were digitized at 4,096 Hz with a National Instruments A/D board using EVAN (custom-designed LabView-based software from Thotec) and analyzed with custom procedures (Wavemetrics, Igor Pro 8). Lower-frequency activity was visualized for 10-min epochs using power spectral densities, which were calculated using the 'dsperiodogram' function of Igor Pro, and spectrograms,

which were generated using the Gabor method on Igor Pro. High-frequency activity up to 650 Hz was visualized by generating Morlet wavelet plots of 0.5–1.0 s epochs of the raw traces used for low-frequency analyses. Inter-spike intervals and spike frequencies were tabulated on Igor Pro using the identical 10-min epochs used above.

Statistical information. Graphical plots and statistical analyses were performed using GraphPad Prism 9 software, unless otherwise indicated. All samples were subjected to Shapiro–Wilk and Kolmogorov–Smirnov normality testing. If the data passed normality by one of these tests, then the data were assumed to be normally distributed. Non-normal samples were analyzed by a two-tailed Mann–Whitney *U* test or Kruskal–Wallis test followed by a Dunn's multiple-comparison test. Normally distributed data were analyzed by a two-tailed Student's *t*-test or ANOVA with post hoc Tukey's multiple-comparison test. No statistical methods were used to predetermine sample sizes, but our sample sizes are similar to those reported in previous publications^{10,11,17–20}. Organoids were generated from hiPSCs or hESCs in batches of 96 organoids per plating. Following quality-control checks, including visual inspection during early differentiation (days 6, 18 and 35), individual organoids were randomly selected from the remaining pool for experiments. Data collection and analysis were not performed blind to the conditions of the experiments. No data points were excluded from the analyses for any reason. Violin plots display the full distribution of individual data points, with dashed and dotted lines indicating the median and quartile values, respectively. Figure legends specify sample numbers and *P* values for all statistical tests. Each *n* value represents an independent experiment. Supplementary Table 4 specifies the number of noncontiguous sections imaged before selection of representative images. The *n* for all other representative images is specified in the figure legends.

Reporting Summary. Further information on research design is available in the Nature Research Reporting Summary linked to this article.

Data availability

Raw and processed scRNA-seq data were deposited at the Gene Expression Omnibus under accession number [GSE165577](https://www.ncbi.nlm.nih.gov/geo/query/acc.cgi?acc=GSE165577). The authors declare that all other data supporting the findings of this study are available within the paper and its Supplementary Information files.

Code availability

CNMF/CNMF-E has been previously published^{29,30} and the original version of CNMF_E is publicly available on GitHub at https://github.com/zhoupc/CNMF_E/. Additional code used in this study is available at https://github.com/SiFTW/CNMF_E_Clustering/.

References

58. Thomson, J. A. et al. Embryonic stem cell lines derived from human blastocysts. *Science* **282**, 1145–1147 (1998).
59. Tchieu, J. et al. Female human iPSCs retain an inactive X chromosome. *Cell Stem Cell* **7**, 329–342 (2010).
60. Roussou, D. L., Gaber, Z. B., Wellik, D., Morrissey, E. E. & Novitch, B. G. Coordinated actions of the forkhead protein Foxp1 and Hox proteins in the columnar organization of spinal motor neurons. *Neuron* **59**, 226–240 (2008).
61. Lee, B. et al. Dlx1/2 and Otp coordinate the production of hypothalamic GHRH- and AgRP-neurons. *Nat. Commun.* **9**, 2026 (2018).
62. Kuwajima, T., Nishimura, I. & Yoshikawa, K. Necdin promotes GABAergic neuron differentiation in cooperation with Dlx homeodomain proteins. *J. Neurosci.* **26**, 5383–5392 (2006).
63. Schindelin, J. et al. Fiji: an open-source platform for biological-image analysis. *Nat. Methods* **9**, 676–682 (2012).
64. Butler, A., Hoffman, P., Smibert, P., Papalexi, E. & Satija, R. Integrating single-cell transcriptomic data across different conditions, technologies, and species. *Nat. Biotechnol.* **36**, 411–420 (2018).
65. Stuart, T. et al. Comprehensive integration of single-cell data. *Cell* **177**, 1888–1902 (2019).
66. Welch, J. D. et al. Single-cell multi-omic integration compares and contrasts features of brain cell identity. *Cell* **177**, 1873–1887 (2019).
67. Yuste, R. et al. A community-based transcriptomics classification and nomenclature of neocortical cell types. *Nat. Neurosci.* **23**, 1456–1468 (2020).
68. Krienen, F. M. et al. Innovations present in the primate interneuron repertoire. *Nature* **586**, 262–269 (2020).
69. Mayer, C. et al. Developmental diversification of cortical inhibitory interneurons. *Nature* **555**, 457–462 (2018).
70. Hodge, R. D. et al. Conserved cell types with divergent features in human versus mouse cortex. *Nature* **573**, 61–68 (2019).
71. Gouwens, N. W. et al. Integrated morphoelectric and transcriptomic classification of cortical GABAergic. *Cell* **183**, 935–953 (2020).
72. Polioudakis, D. et al. A single-cell transcriptomic atlas of human neocortical development during mid-gestation. *Neuron* **103**, 785–801 (2019).

73. Cao, Y. et al. scDC: single-cell differential composition analysis. *BMC Bioinformatics* **20**, 721 (2019).
74. Raudvere, U. et al. g:Profiler: a web server for functional enrichment analysis and conversions of gene lists. *Nucleic Acids Res.* **47**, W191–W198 (2019).
75. Reimand, J., Kull, M., Peterson, H., Hansen, J. & Vilo, J. g:Profiler—a web-based toolset for functional profiling of gene lists from large-scale experiments. *Nucleic Acids Res.* **35**, W193–W200 (2007).
76. Chen, T. W. et al. Ultrasensitive fluorescent proteins for imaging neuronal activity. *Nature* **499**, 295–300 (2013).

Acknowledgements

We thank S. Butler, T. Carmichael and members of the laboratory of B.G.N. for helpful discussions and comments on the manuscript; N. Vishlaghi and F. Turcios-Hernandez for technical assistance, and J. Lee, S.-K. Lee, H. Shinagawa and K. Yoshikawa for valuable reagents. We also thank the UCLA Eli and Edythe Broad Stem Cell Research Center (BSCRC) and Intellectual and Developmental Disabilities Research Center microscopy cores for access to imaging facilities. This work was supported by grants from the California Institute for Regenerative Medicine (CIRM) (DISC1-08819 to B.G.N.), the National Institute of Health (R01NS089817, R01DA051897 and P50HD103557 to B.G.N.; K08NS119747 to R.A.S.; K99HD096105 to M.W.; R01MH123922, R01MH121521 and P50HD103557 to M.J.G.; R01GM099134 to K.P.; R01NS103788 to W.E.L.; R01NS088571 to J.M.P.; R01NS030549 and R01AG050474 to I.M.), and research awards from the UCLA Jonsson Comprehensive Cancer Center and BSCRC Ablon Scholars Program (to B.G.N.), the BSCRC Innovation Program (to B.G.N., K.P. and W.E.L.), the UCLA BSCRC Steffy Brain Aging Research Fund (to B.G.N. and W.E.L.) and the UCLA Clinical and Translational Science Institute (to B.G.N.), Paul Allen Family Foundation Frontiers Group (to K.P. and W.E.L.), the March of Dimes Foundation (to W.E.L.) and the Simons Foundation Autism Research Initiative Bridge to Independence Program (to R.A.S. and M.J.G.). R.A.S. was also supported by the UCLA/NINDS Translational Neuroscience Training Grant (R25NS065723), a Research and Training Fellowship from the American Epilepsy Society, a Taking Flight Award from CURE Epilepsy and a Clinician Scientist training award from the UCLA BSCRC. J.E.B. was supported by the UCLA BSCRC Rose Hills Foundation Graduate Scholarship Training Program. M.W. was supported by postdoctoral training awards provided by the UCLA BSCRC and the Uehara Memorial Foundation. O.A.M. and A.K. were supported in part by the UCLA-California State University Northridge CIRM-Bridges training program (EDUC2-08411). We also acknowledge the support of the IDDRC Cells, Circuits and Systems Analysis, Microscopy and Genetics and Genomics Cores of the Semel Institute of Neuroscience at UCLA, which are supported by the NICHD (U54HD087101 and P50HD10355701). We lastly acknowledge support from a Quantitative and Computational Biosciences Collaboratory Postdoctoral Fellowship to S.M. and the Quantitative and Computational Biosciences Collaboratory community, directed by M. Pellegrini.

Author contributions

R.A.S., O.A.M., A.K., N.N.F. and J.M.P. performed most of the organoid culture experiments, and R.A.S. worked with other authors mentioned below on various analytical procedures. M.W., J.E.B. and B.G.N. assisted with the development of the organoid culture methods. J.E.B., T.F.A. and M.J.G. provided most of the transcriptomic analysis. B.G.N. assisted with imaging analysis. S.M. assisted R.A.S. in computational analysis of calcium indicator imaging experiments. I.F. and I.M. provided expertise in LFP recording methods and data analysis. P.G. provided guidance in two-photon calcium indicator imaging and computational methods. K.P. and W.E.L. provided the hiPSCs from individuals with Rett syndrome used in the experiments. R.A.S., J.M.P. and B.G.N. conceived, designed and supervised the experiments with helpful input from the other authors. R.A.S. and B.G.N. wrote the manuscript with editing help from the other authors.

Competing interests

The use of pifithrin compounds to treat Rett Syndrome and fusion organoids to screen for preclinical efficacy is covered by a patent application filed by the UC Regents with R.A.S., W.E.L. and B.G.N. as inventors. The remaining authors declare no competing interests.

Additional information

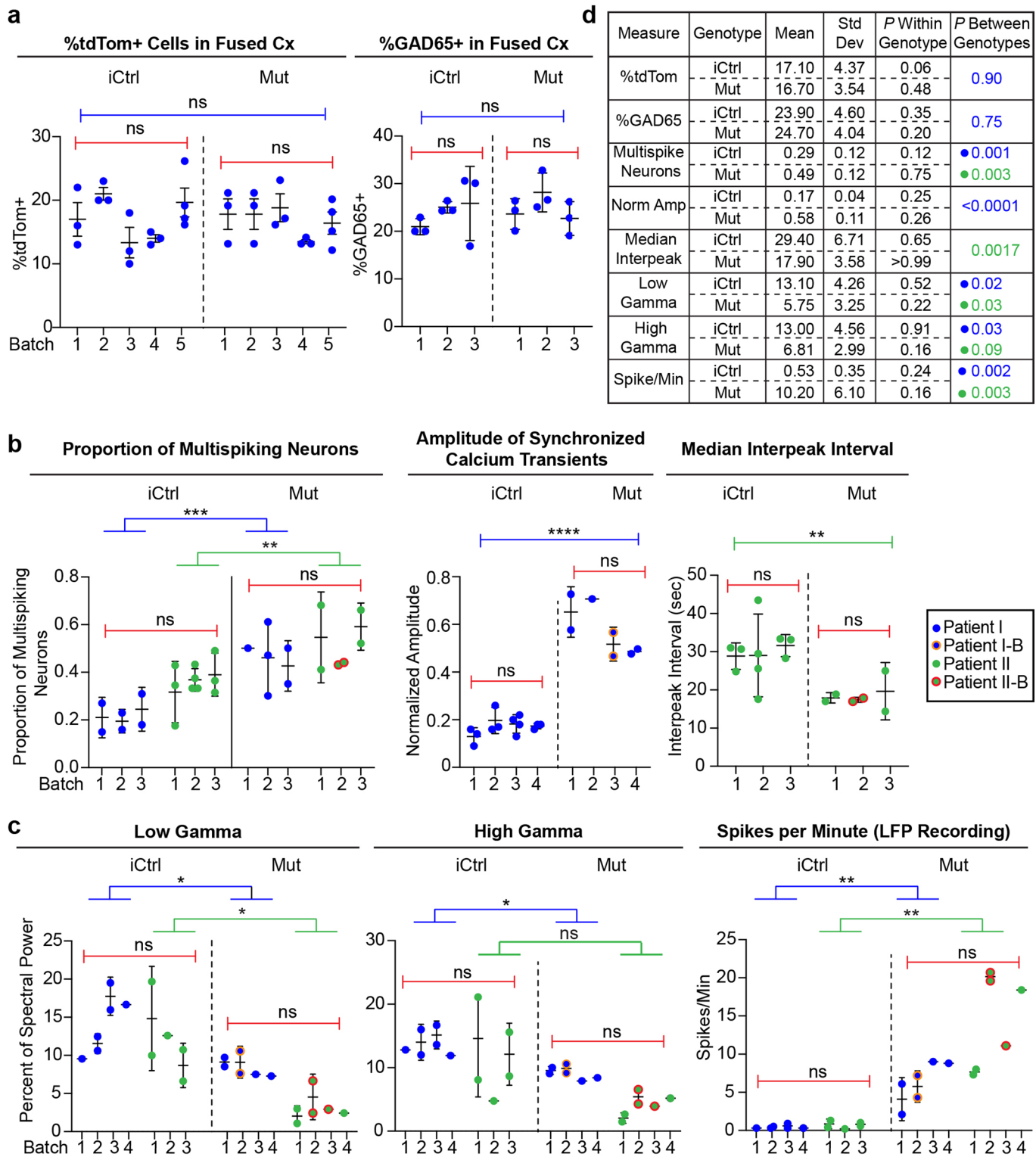
Extended data is available for this paper at <https://doi.org/10.1038/s41593-021-00906-5>.

Supplementary information The online version contains supplementary material available at <https://doi.org/10.1038/s41593-021-00906-5>.

Correspondence and requests for materials should be addressed to B.G.N.

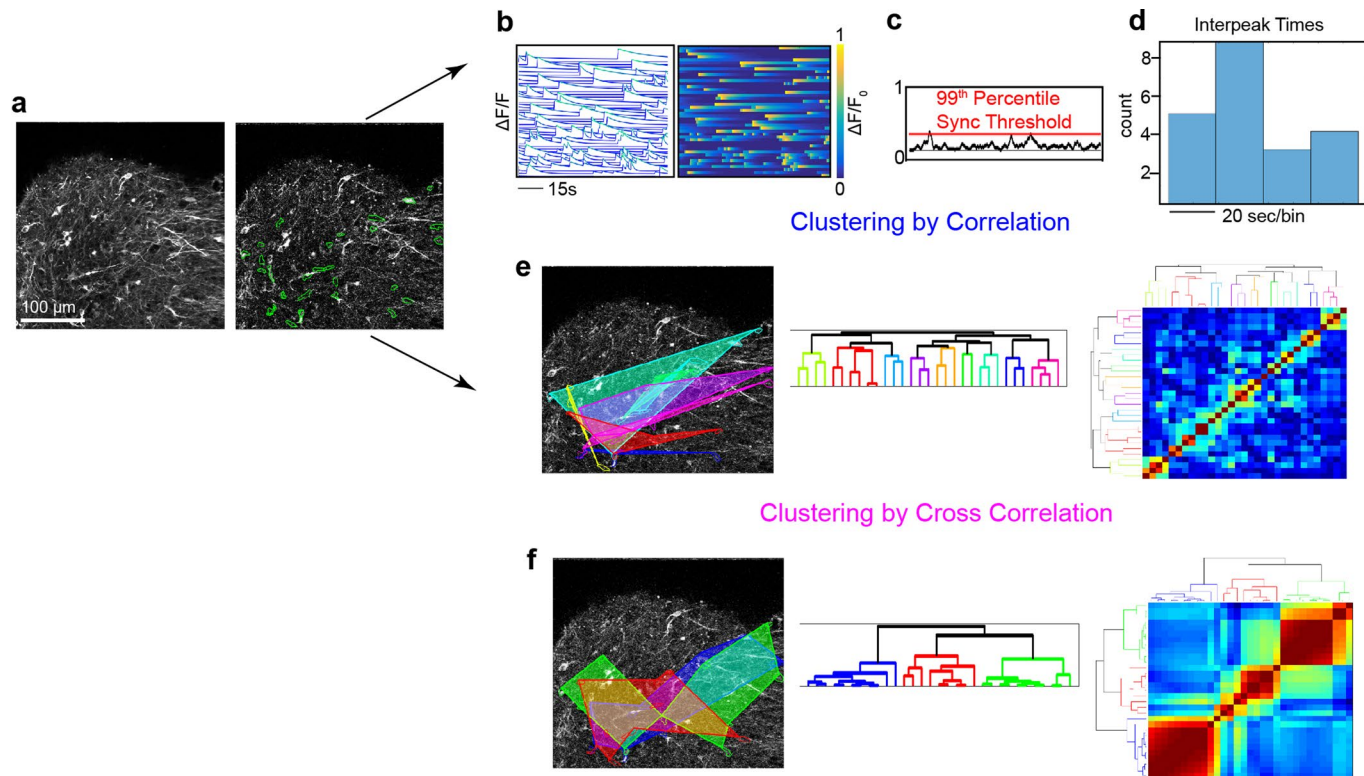
Peer review information *Nature Neuroscience* thanks Benjamin Philpot and the other, anonymous, reviewer(s) for their contribution to the peer review of this work.

Reprints and permissions information is available at www.nature.com/reprints.

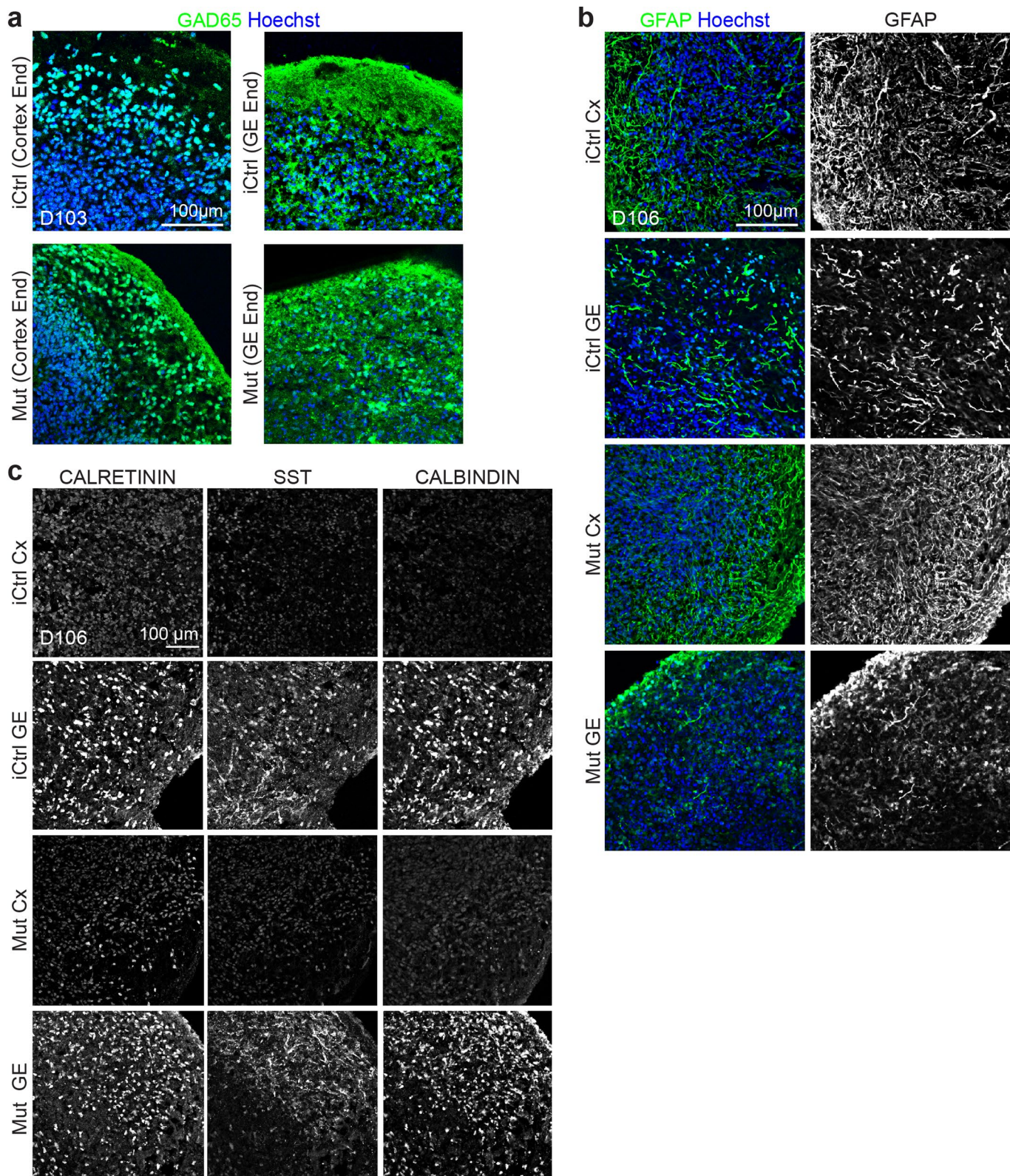


Extended Data Fig. 1 | See next page for caption.

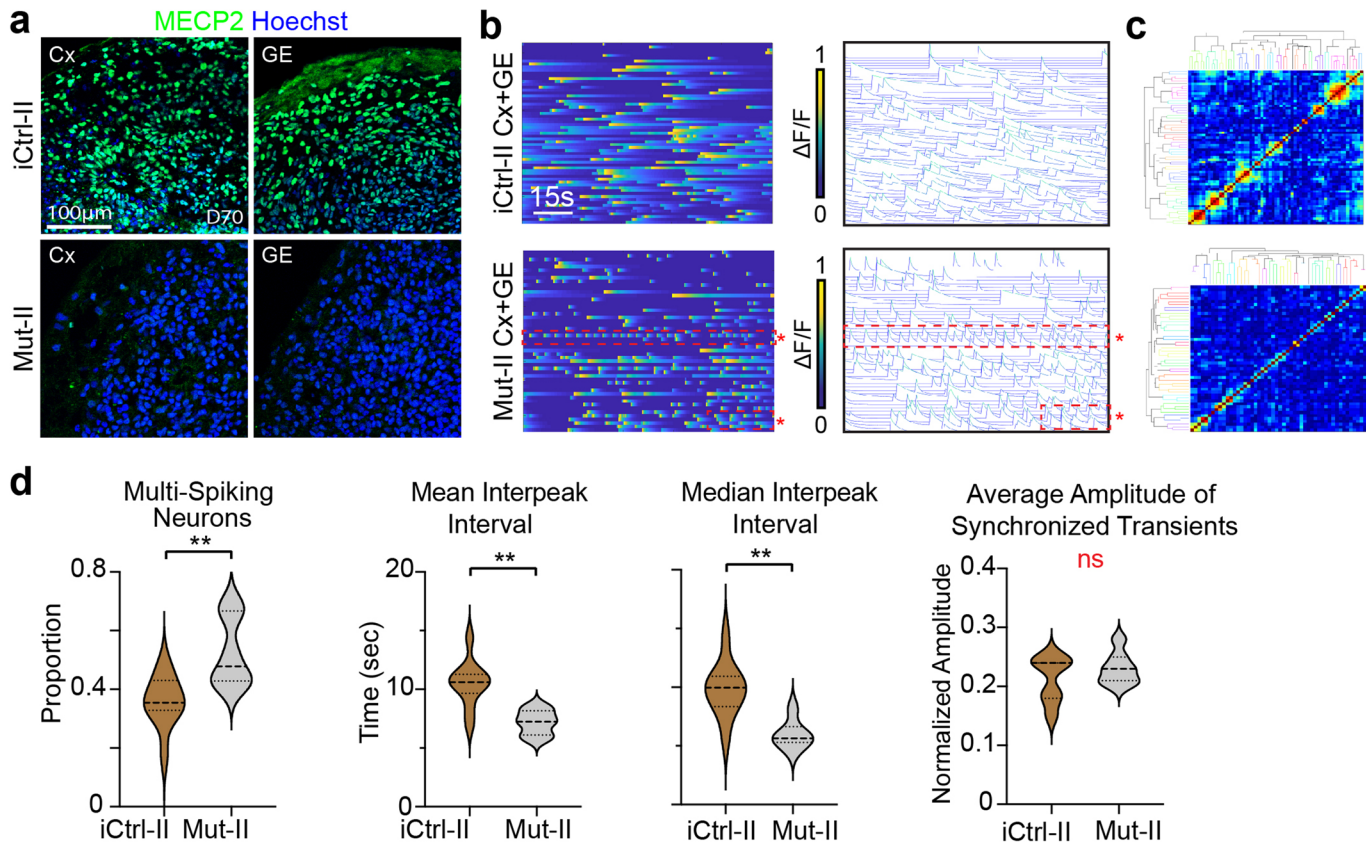
Extended Data Fig. 1 | Plots and table of batch and patient line variability for key experimental measures. **a**, Plots of experimental results from different batches of iCtrl and Mut Cx+GE fusion organoids analyzed for the percentage of cells in the cortical compartment that expressed tdTomato (tdTom) after the GE portion was labeled with AAV1-CAG:tdTom virus (left panel) or GAD65 antibodies (right panel). Each dot represents an individual organoid section used for analysis and numbered elements on the x-axis represent individual experiments. No within- or across-genotype differences were noted for either percentage of Cx expressing tdTom or GAD65. **b,c**, Plots of individual experimental results from iCtrl and Mut Cx+GE fusion calcium indicator and LFP experiments. Each dot represents results from an independent experiment, numbered elements on the x-axis represent independent organoid batches. Blue dots represent hiPSC line I (Rett patient with a 705delG frameshift mutation), green dots represent hiPSC line II (Rett patient with 1461A>G missense mutation), and orange and red circles indicate independently isolated hiPSC lines from the same patient. For calcium indicator and LFP data, plots were generated for *all* experiments in which statistically significant differences between Mut and iCtrl Cx+GE fusions were reported. In all cases in which the same measure resulted in statistically significant differences between Mut and iCtrl in both hiPSC patient lines, the two patient lines were combined for within genotype statistical analyses (for example, proportion of multispiking neurons). **d**, Table with mean, standard deviation (Std Dev), within genotype *P* value, and between genotype *P* value for all measures shown in **a-c**. The results show relatively low Std Dev within genotypes as reflected in non-significant *P* values, yet highly significant differences between the iCtrl and Mut groups in nearly all functional measurements. All between batch statistical analyses were by ANOVA. All between genotype analyses by ANOVA with correction for multiple comparisons by Tukey's test, unless otherwise specified in the main text.



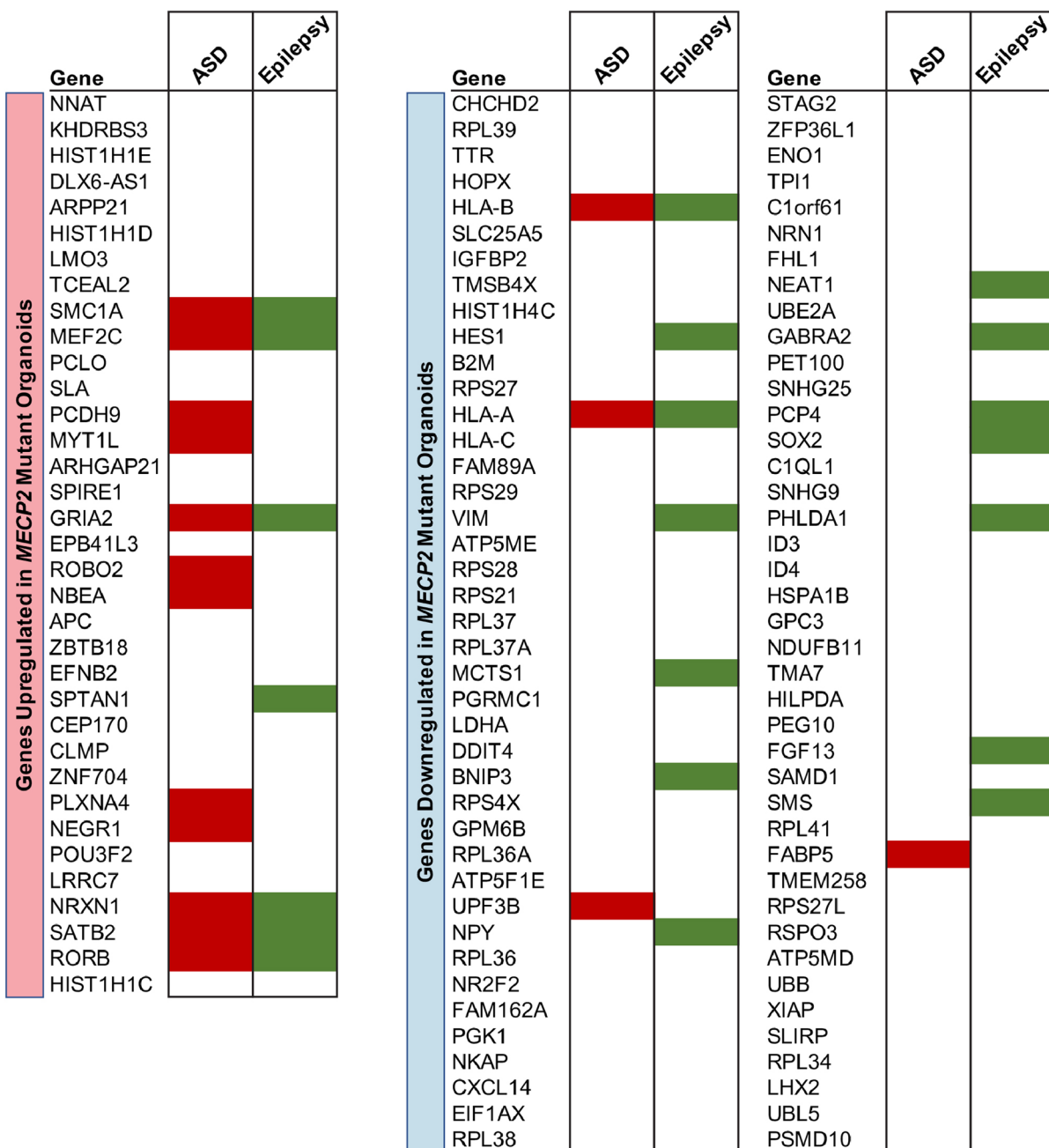
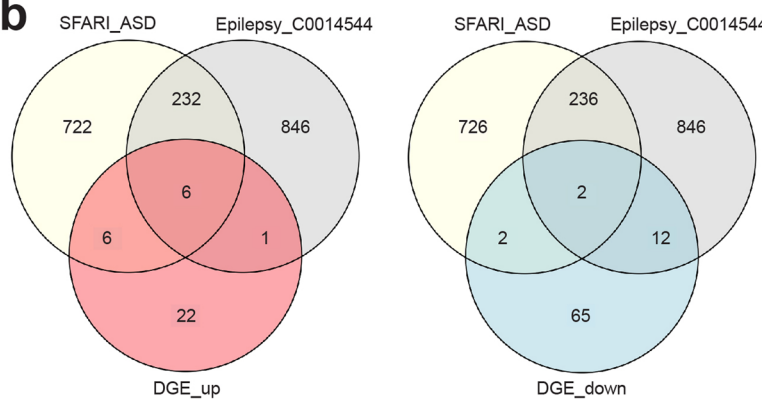
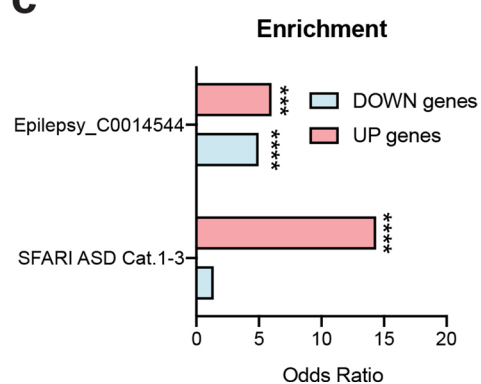
Extended Data Fig. 2 | Constrained non-negative matrix factorization (CNMF) based Ca^{2+} data extraction workflow and output. **a**, Raw image of an GCaMP6f infected Cx+GE organoid (left) and CNMF based identification of fluorescently active (spiking) GCaMP regions of interest (right). **b-d**, Identification and analysis of individual neuronal Ca^{2+} spiking data. **b**, Changes in GCaMP6f fluorescence (normalized $\Delta F/F$) for each neuron in **a** displayed as individual spike trains (left) or the same data displayed as a colorized amplitude plot (right). Individual spiking data are then used to determine various measures of spiking behavior including overall synchronicity based on a threshold level determined following spike shuffling **c** and calculation of interspike intervals **d**. **e**, Simultaneous to **b-d**, Ca^{2+} spiking data are categorized into neuronal microcircuits (clusters) based on correlations between individual Ca^{2+} spikes. **f**, during initial analyses, alternative clustering approaches including cross-correlation was used and the neural microcircuits resulting from multiple approaches were compared to determine the optimal clustering paradigm.



Extended Data Fig. 3 | Immunohistochemical analyses reveal similar cell composition in iCtrl and Mut fusion organoids. **a**, Day -100 iCtrl and Mut Cx+GE fusion organoids have comparable numbers of GAD65⁺ positive cells in both the GE and Cx end (quantification in Fig. 3c). **b**, Both unfused Mut and unfused iCtrl day ~100 GE organoids contain multiple interneuron subtypes including CALRETININ, CALBINDIN, and SOMATOSTATIN (SST) expressing cells. **c**, Mut and iCtrl Day -100 GE and Cx organoids also contain GFAP⁺ astrocytes. All images are representative examples from 3 or more independently imaged sections. See Supplementary Table 4 for additional details.



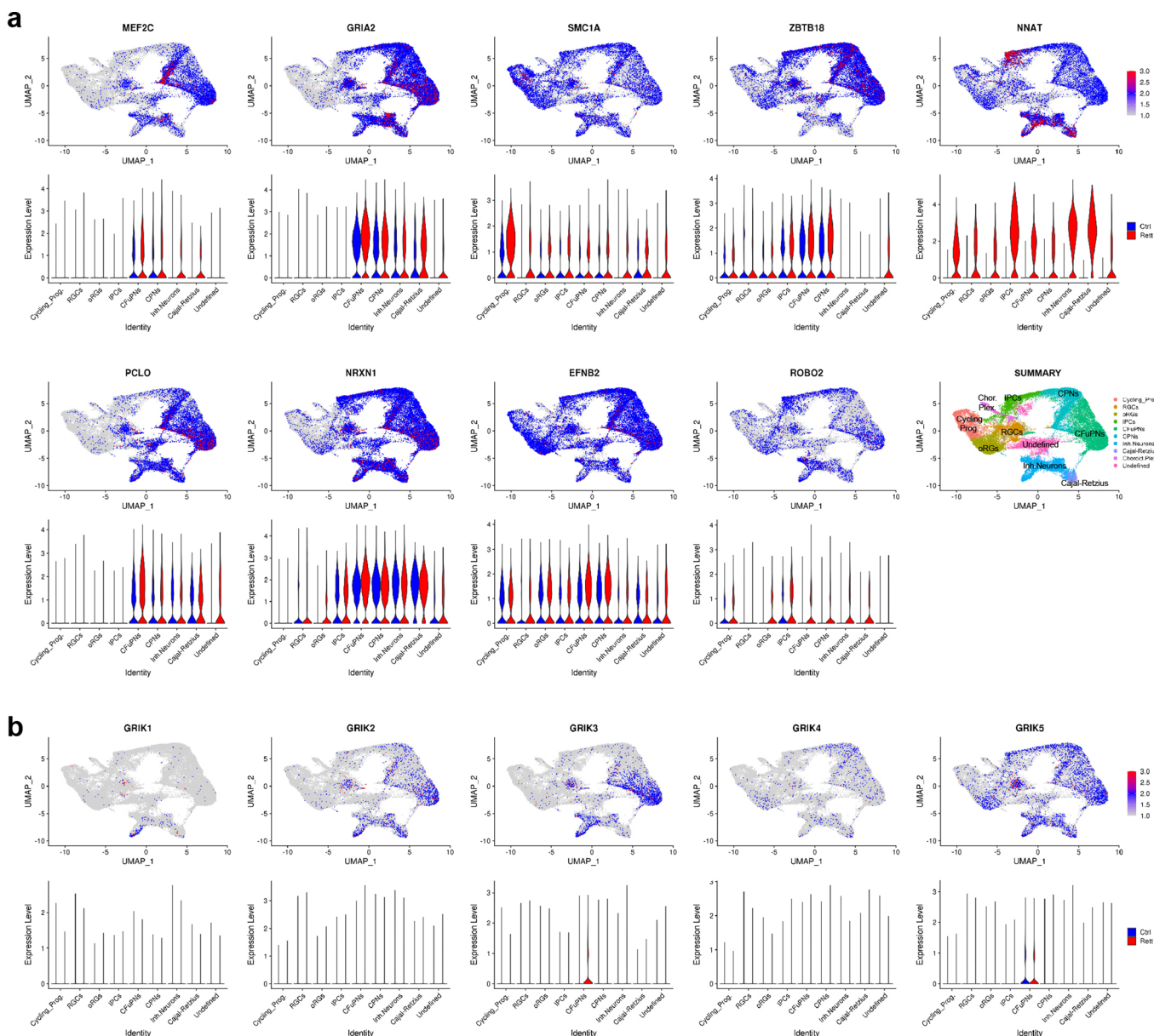
Extended Data Fig. 4 | Rett syndrome fusion organoids from a second patient hiPSC line exhibit neural network irregularities in calcium indicator measurements. **a**, Immunohistochemical analyses of isogenic Cx and GE organoids from a second Rett syndrome patient hiPSC line (harboring a 1461A > G missense mutation, indicated by “II”) reveals either the presence (iCtrl-II) or absence (Mut-II) of MECP2 expression. Representative images from $n=2$ independent experiments and 6 imaged sections. **b**, Mut-II Cx+GE fusions contain hyperexcitable neurons as indicated by the red boxed regions in the bottom $\Delta F/F$ colorized amplitude plot and spike plot. These plots show trains of repeatedly firing Ca^{2+} transients with short interspike intervals that are not present in iCtrl-II Cx+GE (top plots). **c**, There is no discernible change in synchronization of calcium transients between Mut and iCtrl as reflected in the clustergrams. **d**, The hyperexcitable phenotype in Mut-II Cx+GE fusions is reflected in the pooled data both by significant increases in multispike neurons and decreases in mean and median interpeak intervals. Pooled data quantifications, $n=10$ iCtrl-II and $n=6$ Mut-II fusion organoids, where each n is an independently generated organoid. Two-sided Mann-Whitney tests were used, * $P=0.0071$ for the proportion of multispike neurons, ** $P=0.0047$ for the mean interspike interval, ** $P=0.0017$ for the median interspike interval, ns = not significant. Plot in **d** displays the full distribution of individual data points with dotted lines indicating the median and quartile values.

a**b****c**

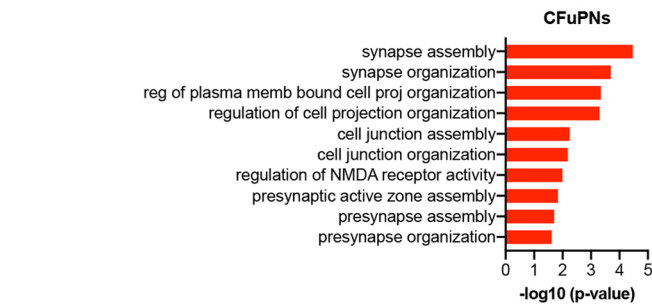
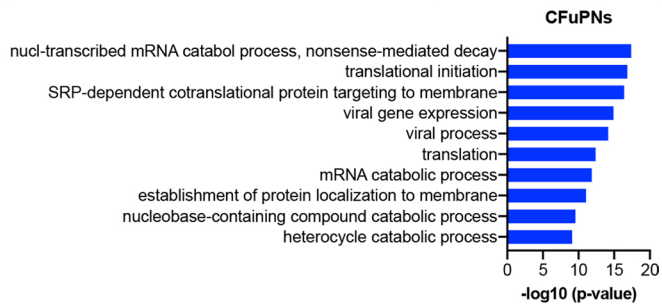
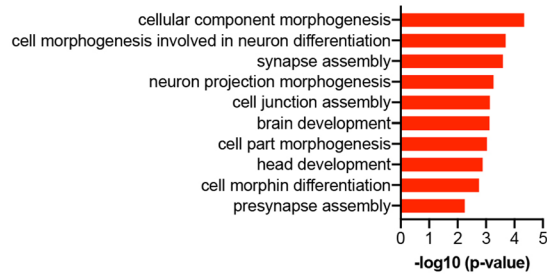
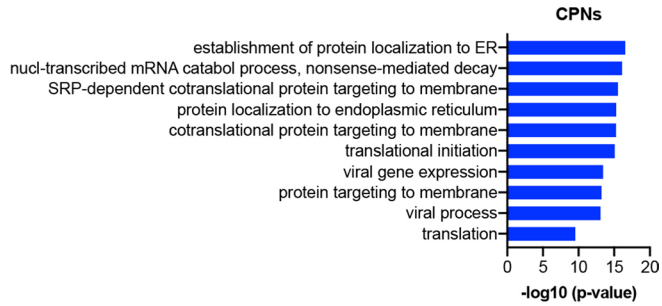
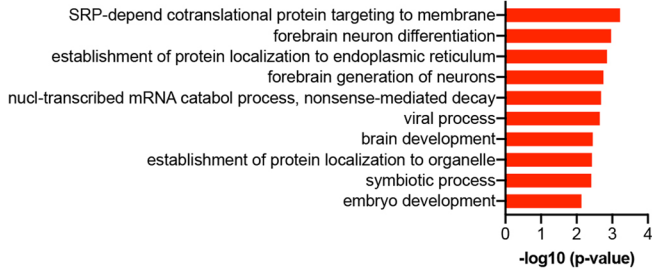
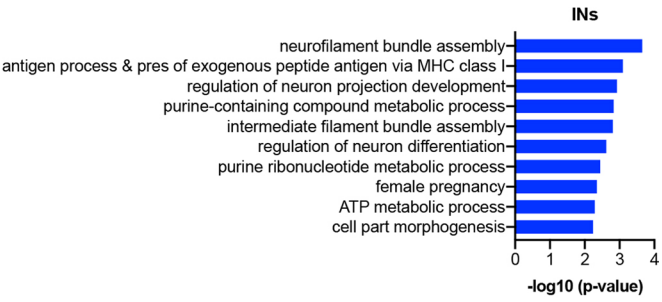
Extended Data Fig. 5 | See next page for caption.

Extended Data Fig. 5 | Enrichment of autism and epilepsy risk genes in up/downregulated genes in MECP2 mutant and isogenic control organoids.

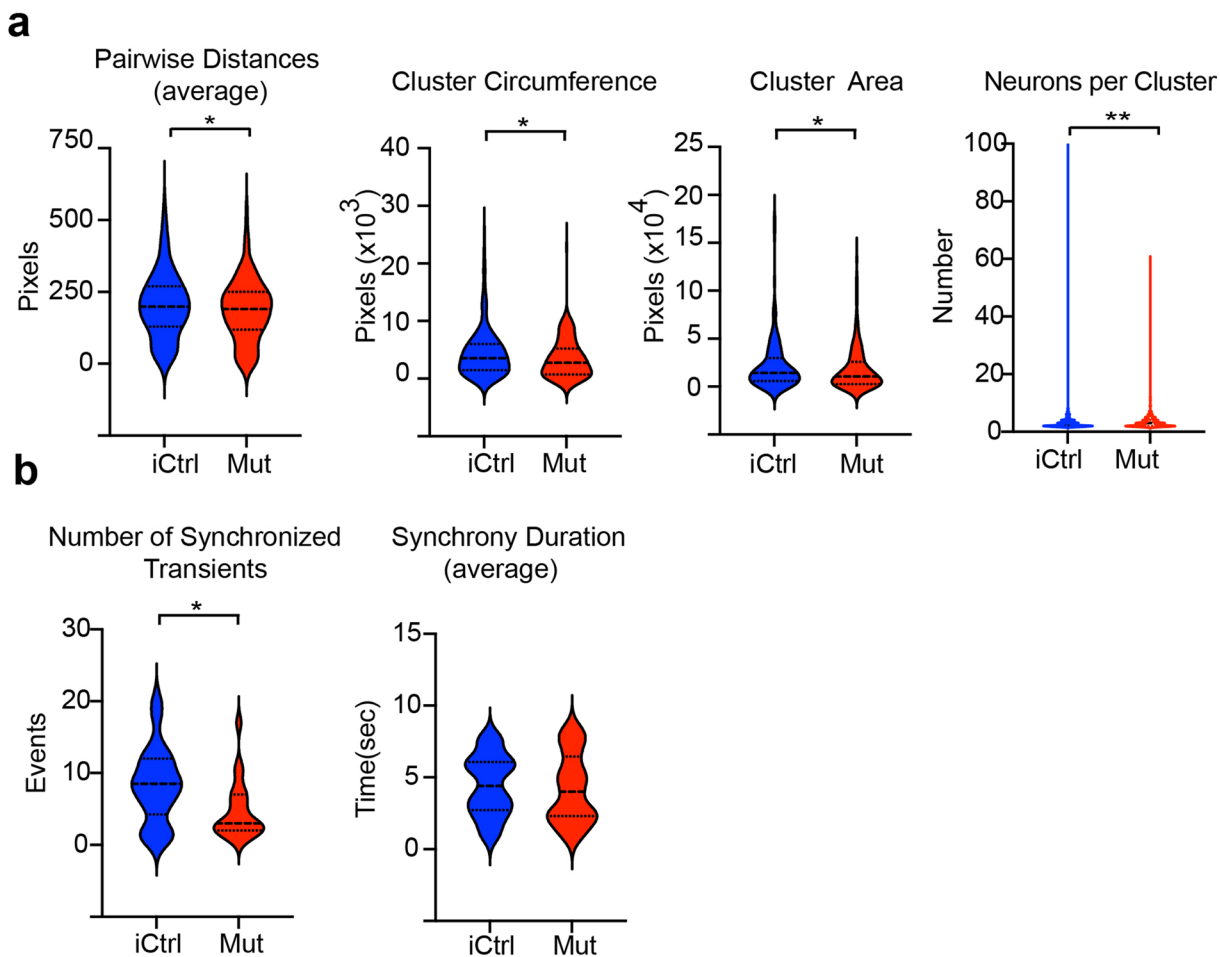
a, Overlap of differentially expressed genes in MECP2 mutant organoids (all cell groups) with SFARI autism spectrum disorder (ASD) gene categories 1-3 and DisGeNET epilepsy Gene-Disease Association list (CUI: C0014544). Overlaps between data are indicated by red and green shading and displayed as Venn diagrams in **b**. **c**, Two-sided Fisher's Exact Test was used to determine if Up/Downregulated genes show enrichment for genes in SFARI and epilepsy gene lists. Odds ratio from the test are displayed along with Bonferroni-corrected *P* values. Up/Epilepsy: ****P*=0.0016, Down/Epilepsy: *****P*=1.81×10⁻⁵, Up/ASD: *****P*=5.72×10⁻⁹, Down/ASD: *P*=1.00.



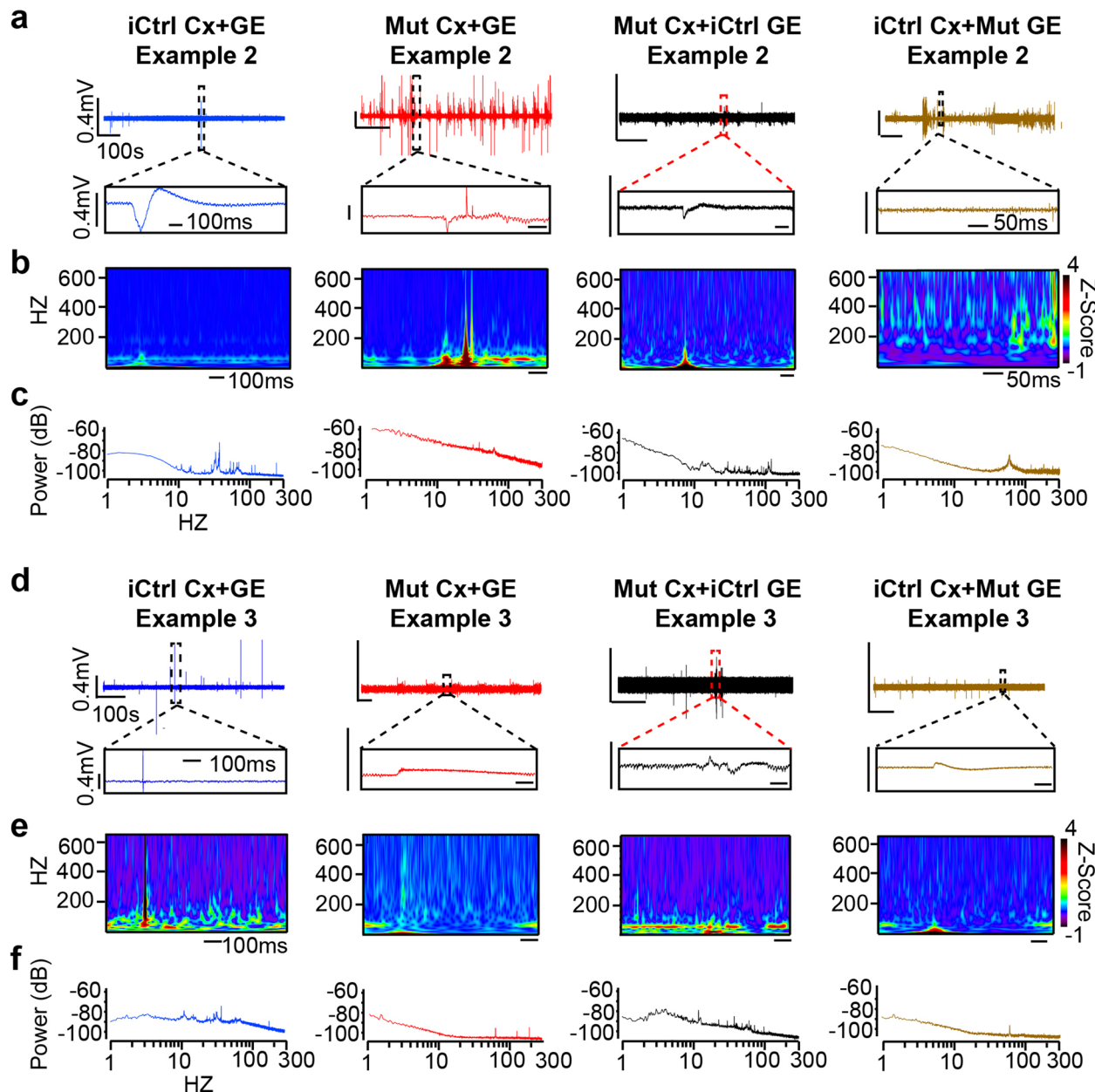
Extended Data Fig. 6 | UMAP representation of select genes associated with synaptogenesis and kainate responsiveness. **a**, UMAP representation of select genes associated with axonal projections and synaptogenesis found to be upregulated in *MECP2* mutant Cx+GE fusion organoids. Violin plots display the relative expression level of each gene across the indicated cell clusters. **b**, UMAP representation of kainate receptor gene expression within the Cx+GE fusion organoids.

Terms Associated with Genes Increased in *MECP2* Mut Organoids**Terms Associated with Genes Decreased in *MECP2* Mut Organoids****CPNs****CPNs****INs****INs**

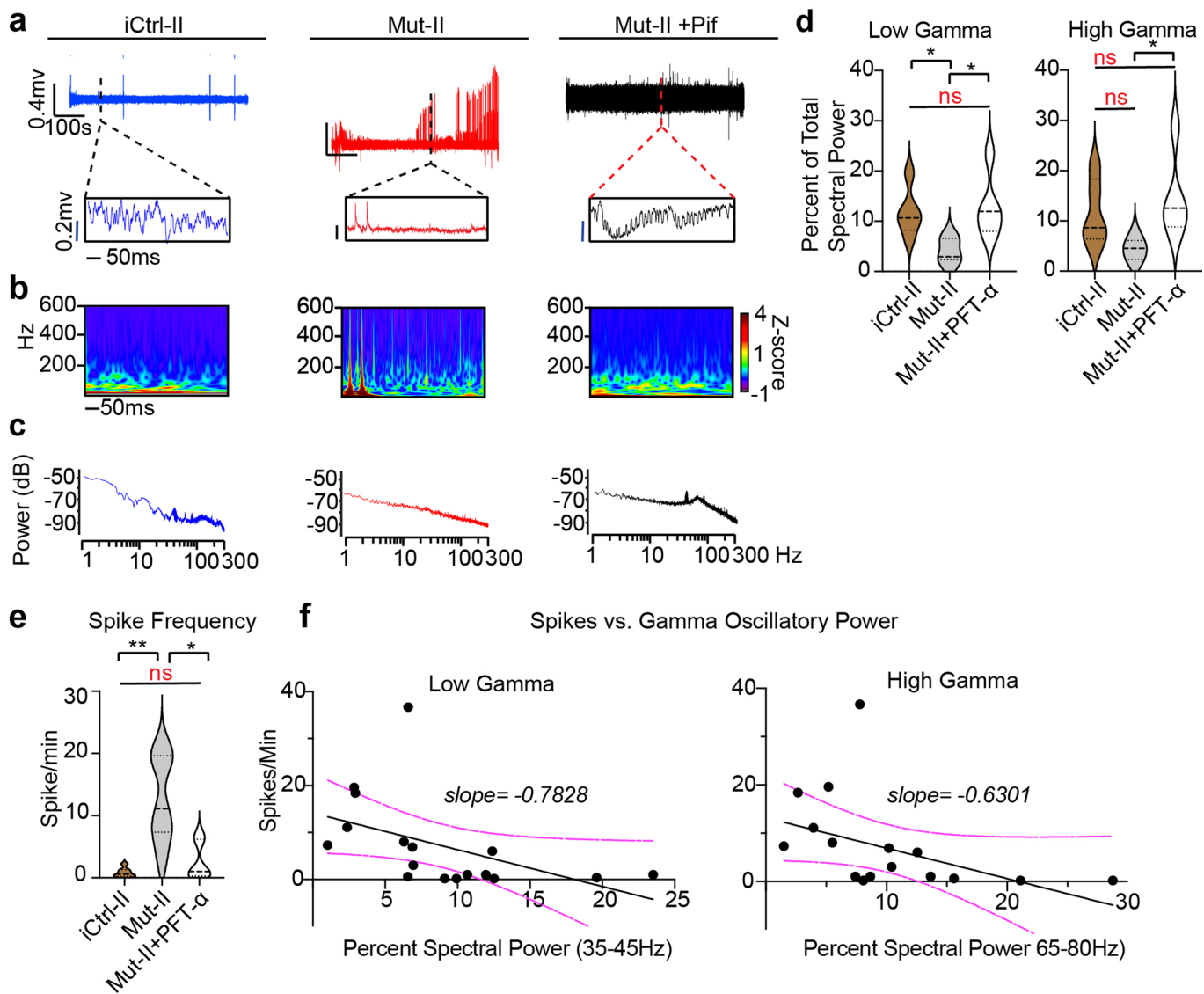
Extended Data Fig. 7 | Gene ontology analysis of neuronal subtype clusters. Top 10 most enriched Gene Ontology biological process (GO BP) terms associated with upregulated or downregulated differentially expressed genes when comparing Mut and iCtrl within the main excitatory (CPN and CFuPN) and interneuron (IN) clusters. Upregulated genes in the excitatory clusters are highly enriched for terms associated with synaptogenesis and axonal morphogenesis while downregulated genes are associated with mRNA catabolism and translation. In contrast, synaptogenesis terms are absent among the upregulated genes in the IN cluster, with this set populated by terms associated with forebrain differentiation and axonal morphogenesis. Downregulated genes in the IN cluster are enriched for metabolism and cellular cytoskeleton associated terms.



Extended Data Fig. 8 | Spatially restricted microcircuit clusters and fewer synchronous events in MECP2 Mut Cx + GE organoids. **a**, Pooled data for neuronal clusters derived here using Ca^{2+} activity correlations, reveal spatially restricted (smaller) microcircuit clusters with fewer average neurons per cluster in Mut compared to iCtrl. **b**, Pooled data of synchronous events demonstrates a reduced number of events, but with each event having a significantly higher amplitude (Fig. 6), in Mut compared to iCtrl. Synchronous events have similar overall duration in both conditions ($n=6$ for iCtrl, $n=7$ for Mut and represents independently generated organoids, $*P=0.0436$ for Pairwise Distances, $*P=0.0203$ for Cluster Circumference, $*P=0.0321$ for Cluster Area, $**P=0.0089$ for Neurons per Cluster, and $*P=0.0180$ for Number of Synchronized Transients). Plots display the full distribution of individual data points with dotted lines to indicate the median and quartile values. Following a normality test, statistical significance was determined using a two-sided Mann-Whitney *U*-test.



Extended Data Fig. 9 | Additional independent examples of local field potential recordings. **a,d**, Representative raw 10-minute LFP traces (top) and time expanded segments (bottom) from either unmixed iCtrl or Mut Cx+GE fusion organoids, or Mut Cx+iCtrl GE or iCtrl Cx+Mut GE mixed fusion organoids. **b,e**, Morlet plots derived from the time expanded segments shown in **a,d**. **c,f**, Periodogram derived from the entire 10 min traces shown in **a,d**.



Extended Data Fig. 10 | Rett syndrome fusion organoids from a second patient hiPSC line demonstrate epileptiform changes in extracellular recordings.

a, Raw trace of a representative 10-minute LFP recording (top) and time expanded window (bottom) from iCtrl-II, Mut-II, or Mut-II + PFT- α Cx+GE fusion organoids. **b**, Morlet plots showing high frequency activity associated with the time expanded segments shown in **a**. **c**, Periodograms derived from the entire recordings shown in **a**. **d**, Quantification of high and low gamma spectral power from LFP recordings demonstrates a significant decrease in low gamma power and a sizeable but non-significant loss of high gamma power in Mut-II Cx+GE fusions. PFT- α treatment of Mut-II Cx+GE fusions results in a statistically significant rescue of both low and high gamma oscillatory power. Low gamma; Ordinary ANOVA, overall $P=0.0024$, Tukey's Multiple comparisons, $*P=0.0313$ iCtrl II vs Mut II, $*P=0.0211$ Mut II vs Mut II + PFT. High gamma; Ordinary ANOVA, overall $P=0.0091$, Tukey's multiple comparisons, $*P=0.0243$ Mut II vs Mut II + PFT, $P=0.09$ between iCtrl-II and Mut. **e**, Spike frequency across multiple independent experiments Kruskal-Wallis test, overall $P=0.0003$, Dunn's multiple comparisons $**P=0.0028$, $*P=0.0276$. For **d** and **e**, $n=5$ for iCtrl-II and Mut-II + PFT- α , $n=6$ for Mut-II (total $n=16$). **f**, Plots of high and low gamma spectral power versus spike frequency demonstrates an inverse relationship between gamma power and spiking. The solid black line is the best fit following linear regression, and the dashed magenta lines indicate 95% confidence intervals for the estimated line of best fit. The slope of the line of best fit is indicated above each graph. Plots in **d** and **e** display the full distribution of individual data points with dotted lines to indicate the median and quartile values.

Reporting Summary

Nature Portfolio wishes to improve the reproducibility of the work that we publish. This form provides structure for consistency and transparency in reporting. For further information on Nature Portfolio policies, see our [Editorial Policies](#) and the [Editorial Policy Checklist](#).

Statistics

For all statistical analyses, confirm that the following items are present in the figure legend, table legend, main text, or Methods section.

n/a Confirmed

- The exact sample size (n) for each experimental group/condition, given as a discrete number and unit of measurement
- A statement on whether measurements were taken from distinct samples or whether the same sample was measured repeatedly
- The statistical test(s) used AND whether they are one- or two-sided
Only common tests should be described solely by name; describe more complex techniques in the Methods section.
- A description of all covariates tested
- A description of any assumptions or corrections, such as tests of normality and adjustment for multiple comparisons
- A full description of the statistical parameters including central tendency (e.g. means) or other basic estimates (e.g. regression coefficient) AND variation (e.g. standard deviation) or associated estimates of uncertainty (e.g. confidence intervals)
- For null hypothesis testing, the test statistic (e.g. F , t , r) with confidence intervals, effect sizes, degrees of freedom and P value noted
Give P values as exact values whenever suitable.
- For Bayesian analysis, information on the choice of priors and Markov chain Monte Carlo settings
- For hierarchical and complex designs, identification of the appropriate level for tests and full reporting of outcomes
- Estimates of effect sizes (e.g. Cohen's d , Pearson's r), indicating how they were calculated

Our web collection on [statistics for biologists](#) contains articles on many of the points above.

Software and code

Policy information about [availability of computer code](#)

Data collection	Publicly available ImageJ/Fiji version 2.00 for 2-photon calcium imaging; Zeiss Zen 2.3 (Blue and Black editions) and Zen 2011 (Black edition) for confocal image collection, custom built "Evan" from Thotec for LFP acquisition.
Data analysis	Igor Pro v8 (LFP data), MATLAB 2016b (calcium analysis), Bitplane Imaris 9.3 and 9.5 (synaptic staining analysis), GraphPad Prism v9 (statistics and graphical plots), Adobe Photoshop and Illustrator 2019, 2020, 2021 (image processing and composite compilations), and R v4.03 (single cell RNAseq), original CNMF-E code is available at https://github.com/zhoup/CNMF_E , customizations to CNMF-E is available at https://github.com/SiFTW/CNMF_EClustering/ .

For manuscripts utilizing custom algorithms or software that are central to the research but not yet described in published literature, software must be made available to editors and reviewers. We strongly encourage code deposition in a community repository (e.g. GitHub). See the Nature Portfolio [guidelines for submitting code & software](#) for further information.

Data

Policy information about [availability of data](#)

All manuscripts must include a [data availability statement](#). This statement should provide the following information, where applicable:

- Accession codes, unique identifiers, or web links for publicly available datasets
- A description of any restrictions on data availability
- For clinical datasets or third party data, please ensure that the statement adheres to our [policy](#)

Raw and processed single-cell RNA sequencing data were deposited at the Gene Expression Omnibus with accession number GSE165577. The authors declare that all other data supporting the findings of this study are available within the paper and its supplementary information files.

Field-specific reporting

Please select the one below that is the best fit for your research. If you are not sure, read the appropriate sections before making your selection.

Life sciences Behavioural & social sciences Ecological, evolutionary & environmental sciences

For a reference copy of the document with all sections, see nature.com/documents/nr-reporting-summary-flat.pdf

Life sciences study design

All studies must disclose on these points even when the disclosure is negative.

Sample size	No methods were used to pre-determine sample sizes. Minimum samples sizes were determined based on previously published studies, and for all experiments at least three independently generated samples were used. This number is specified in the figure legends.
Data exclusions	No data were excluded. Once statistical significance was reached for a particular analysis (eg spike frequency from LFP data), further analysis of this type was not performed even if additional LFP recordings were performed to obtain data for distinct analyses (eg counts of gamma activity).
Replication	Experiments were conducted using multiple independent batches of organoids derived from H9 hESC, isogenic MECP2 mutant (Mut) and wild-type control hiPSC lines from two independent patients. In addition, two independently generated hiPSC lines were used for each patient, where available. For all analyses, organoids from at least 3 independent differentiations were utilized. In most cases, including all physiologic analyses, at least 5 independent organoid samples and upwards of 12, were sampled.
Randomization	Following visualization at multiple points during development (e.g., age day 12, 18, 35, and 56) to ensure expected formation of neural rosette structure , brain organoids were randomly selected for fusion. Fused organoids were then randomly selected for experiments.
Blinding	Blinding was not routinely performed as knowledge of experimental conditions was often required during data collection and analyses. Where applicable, control and mutant groups were routinely processed and imaged in parallel using the same conditions/parameters to reduce bias.

Reporting for specific materials, systems and methods

We require information from authors about some types of materials, experimental systems and methods used in many studies. Here, indicate whether each material, system or method listed is relevant to your study. If you are not sure if a list item applies to your research, read the appropriate section before selecting a response.

Materials & experimental systems	Methods
n/a	Involved in the study
<input type="checkbox"/>	<input checked="" type="checkbox"/> Antibodies
<input type="checkbox"/>	<input checked="" type="checkbox"/> Eukaryotic cell lines
<input checked="" type="checkbox"/>	<input type="checkbox"/> Palaeontology and archaeology
<input checked="" type="checkbox"/>	<input type="checkbox"/> Animals and other organisms
<input checked="" type="checkbox"/>	<input type="checkbox"/> Human research participants
<input checked="" type="checkbox"/>	<input type="checkbox"/> Clinical data
<input checked="" type="checkbox"/>	<input type="checkbox"/> Dual use research of concern
n/a	Involved in the study
	<input checked="" type="checkbox"/> ChIP-seq
	<input checked="" type="checkbox"/> Flow cytometry
	<input checked="" type="checkbox"/> MRI-based neuroimaging

Antibodies

Antibodies used	Primary antibodies used include the following: goat anti-BRN2 (POU3F2; Santa Cruz Biotechnology sc-6029), 1:4000 mouse anti-CALBINDIN (Clone CB-955, Sigma-Aldrich C9848), 1:5000 rabbit anti-CALRETININ (EMD Millipore AB5054), 1:500 rabbit anti-Cleaved Caspase-3 (Asp175) (Cell Signaling 9661) 1:2000 rat anti-CTIP2 (BCL11B; Abcam ab18465), 1:1000 rabbit anti-DLX1 (generous gift of Drs. Soo Kyung Lee and Jae Lee, University of Buffalo), 1:3000 guinea pig anti-DLX2 (generous gift of Drs. Kazuaki Yoshikawa and Hideo Shinagawa, BioAcademia 74-116), 1:3000 guinea pig anti-DLX5 (generous gift of Drs. Kazuaki Yoshikawa and Hideo Shinagawa, BioAcademia 74-117), 1:3000 rabbit anti-FOXP1 (Abcam ab18259), 1:1000 rabbit anti-GABA (Sigma-Aldrich A2052), 1:10000 mouse anti-GAD65 (BD Biosciences 559931), 1:200 mouse anti-GEPRYRIN (Synaptic Systems 147021), 1:500 goat anti-LHX2 (C-20, Santa Cruz Biotechnology sc-19344), 1:1000 mouse anti-N-CADHERIN (CDH2, BD Biosciences 610920), 1:800
-----------------	--

rabbit anti-Neuropeptide Y (EMD Millipore, AB10980), 1:1000
 mouse anti-NKX2.1 (Novocastra NCL-L-TTR-1), 1:500
 mouse anti-PAX6 (Developmental Studies Hybridoma Bank), 1:100
 rabbit anti-PAX6 (MBL International PD022), 1:1000
 mouse anti-PSD95 (Millipore MAB1598), 1:1000
 mouse anti-SATB2 (Abcam ab51502), 1:100
 goat anti-SOX2 (Santa Cruz Biotechnology sc-17320, 1:100
 rat anti-SOMATOSTATIN (SST, EMD Millipore MAB354), 1:100
 rabbit anti-TBR1 (Abcam ab31940), 1:2000
 chicken anti-TBR2 (EOMES; EMD Millipore AB15894), 1:1000
 rabbit anti-tubulin B3 (TUBB3, BioLegend, 802001), 1:1000
 guinea pig anti-VGAT (Synaptic Systems 131004), 1:1000
 guinea pig anti-VGLUT1 (SLC17A7; EMD Millipore AB5905), 1:1000.

Secondary antibody staining was conducted using the following antibodies:

Fluorescein (FITC)-conjugated Donkey anti-Chicken IgY (Jackson Immunoresearch 703-095-155), 1:500
 Alexa Fluor 488-conjugated Donkey anti-Chicken IgY (Jackson Immunoresearch 703-545-155), 1:1000
 Cy3-conjugated Donkey anti-Chicken IgY (Jackson Immunoresearch 703-165-155), 1:1000
 Cy5-conjugated Donkey anti-Chicken IgY (Jackson Immunoresearch 703-175-155), 1:700

DyLight 405-conjugated Donkey anti-Goat IgG (Jackson Immunoresearch 705-545-147), 1:1000
 Alexa Fluor 488-conjugated Donkey anti-Goat IgG (Jackson Immunoresearch 705-545-147), 1:1000
 Cy3-conjugated Donkey anti-Goat IgG (Jackson Immunoresearch 705-165-147), 1:1000
 Alexa Fluor 594-conjugated Donkey anti-Goat IgG (Jackson Immunoresearch 705-585-147), 1:1000
 Alexa Fluor 647-conjugated Donkey anti-Goat IgG (Jackson Immunoresearch 705-605-147), 1:1000

Fluorescein (FITC)-conjugated Donkey anti-Guinea Pig IgG (Jackson Immunoresearch 706-095-148), 1:500
 Alexa Fluor 488-conjugated Donkey anti-Guinea Pig IgG (Jackson Immunoresearch 706-545-148), 1:1000
 Cy3-conjugated Donkey anti-Guinea Pig IgG (Jackson Immunoresearch 706-165-148), 1:1000
 Alexa Fluor 594-conjugated Donkey anti-Guinea Pig IgG (Jackson Immunoresearch 706-585-148), 1:1000
 Alexa Fluor 647-conjugated Donkey anti-Guinea Pig IgG (Jackson Immunoresearch 706-605-148), 1:1000

Dylight 405-conjugated Donkey anti-Mouse IgG (Jackson Immunoresearch 715-475-151), 1:1000
 Alexa Fluor 488-conjugated Donkey anti-Mouse IgG (Jackson Immunoresearch 715-545-151), 1:1000
 Cy3-conjugated Donkey anti-Mouse IgG (Jackson Immunoresearch 715-165-150), 1:1000
 Cy3-conjugated Donkey anti-Mouse IgG (Jackson Immunoresearch 715-165-151), 1:1000
 Alexa Fluor 647-conjugated Donkey anti-Mouse IgG (Jackson Immunoresearch 715-605-150), 1:1000
 Alexa Fluor 488 Goat anti-Mouse IgG1 Cross-Adsorbed (Invitrogen A21121), 1:1000
 Alexa Fluor 594 Goat anti-Mouse IgG2a Cross-Adsorbed (Invitrogen A21135), 1:1000

DyLight 405-conjugated Donkey anti-Rabbit IgG (Jackson Immunoresearch 711-475-152), 1:1000
 Alexa Fluor 488-conjugated Donkey anti-Rabbit IgG (Jackson Immunoresearch 711-545-152), 1:1000
 Cy3-conjugated Donkey anti-Rabbit IgG (Jackson Immunoresearch 711-165-152), 1:1000
 Alexa Fluor 594-conjugated Donkey anti-Rabbit IgG (Jackson Immunoresearch 711-585-152), 1:1000
 Alexa Fluor 647-conjugated Donkey anti-Rabbit IgG (Jackson Immunoresearch 711-605-152), 1:1000

Alexa Fluor 488-conjugated Donkey anti-Rat IgG (Jackson Immunoresearch 712-545-153), 1:1000
 Cy3-conjugated Donkey anti-Rat IgG (Jackson Immunoresearch 712-165-153), 1:1000
 Alexa Fluor 594-conjugated Donkey anti-Rat IgG (Jackson Immunoresearch 712-585-153), 1:1000
 Alexa Fluor 647-conjugated Donkey anti-Rat IgG (Jackson Immunoresearch 712-605-153), 1:1000

Fluorescein (FITC)-conjugated Donkey anti-Sheep IgG (Jackson Immunoresearch 713-095-147), 1:1000
 Cy3-conjugated Donkey anti-Sheep IgG (Jackson Immunoresearch 713-165-147), 1:1000
 Alexa Fluor 647-conjugated Donkey anti-Sheep IgG (Jackson Immunoresearch 713-605-147), 1:1000.

Validation

All antibodies were selected based on their known or predicted recognition of human proteins, and demonstrated specificity and quality as shown in previous citations. The indicated number of citations is taken from the antibody database www.citeab.com. For antibodies with limited or no previous citations, antibodies were also tested on mouse and/or human brain sections and patterns compared to mRNA expression patterns revealed by *in situ* hybridization. For investigator-produced antibodies for which RRID and/or CiteAb listings were available, a link to the study in which the antibody was first described is provided.

The following primary antibodies were used; [M,H] indicate species (Mouse/Human) for which the antibody has been previously used:

goat anti-BRN2 (POU3F2; Santa Cruz Biotechnology sc-6029), RRID:AB_2300359, 49 citations [M,H]
 mouse anti-CALBINDIN (Clone CB-955, Sigma-Aldrich C9848), RRID:AB_476894, 429 citations [M,H]
 rabbit anti-CALRETININ (EMD Millipore AB5054), RRID: AB_2068506, 189 citations [M,H]
 rabbit anti-Cleaved Caspase-3 (Asp175) (Cell Signaling 9661), 5734 citations [M,H]
 rat anti-CTIP2 (BCL11B; Abcam ab18465), 1:1000; RRID:AB_2064130, 543 citations [M,H]
 rabbit anti-DLX1; validated in <https://doi.org/10.1038/s41467-018-04377-4> [M]
 guinea pig anti-DLX2; validated in <https://doi.org/10.1523/JNEUROSCI.1262-06.2006> [M]
 guinea pig anti-DLX5 validated in <https://doi.org/10.1523/JNEUROSCI.1262-06.2006> [M]
 rabbit anti-FOGX1 (Abcam ab18259), RRID:AB_732415, 84 citations [M,H]
 rabbit anti-GABA (Sigma-Aldrich A2052), RRID:AB_477652, 497 citations [M,H]
 mouse anti-GAD65 (BD Biosciences 559931), RRID:AB_397380, 14 citations [M]
 mouse anti-GEPHYRIN (Synaptic Systems 147021), RRID:AB_2232546, 65 citations [M]
 goat anti-LHX2 (C-20, Santa Cruz Biotechnology sc-19344), RRID:AB_2135660, 29 citations [M]

mouse anti-N-CADHERIN (CDH2, BD Biosciences 610920), RRID:AB_2077527, 392 citations [M,H]
 rabbit anti-Neuropeptide Y (Abcam, ab10980), RRID:AB_297635, 21 citations [M, H]
 mouse anti-NKX2.1 (Leica/Novocastra NCL-L-TTR-1), RRID:AB_564042, 2 citations [H]
 mouse anti-PAX6 (Developmental Studies Hybridoma Bank), RRID:AB_528427, 627 citations [M,H]
 rabbit anti-PAX6 (MBL International PD022), RRID:AB_1520876, 9 citations [M]
 mouse anti-PSD95 (Millipore MAB1598), RRID:AB_11212185, 72 citations [M,H]
 mouse anti-SATB2 (Abcam ab51502), RRID:AB_882455, 191 citations [M,H]
 goat anti-SOX2 (Santa Cruz Biotechnology sc-17320, RRID:AB_2286684, 482 citations [M,H]
 rat ant-SOMATOSTATIN (SST, EMD Millipore MAB354), RRID:AB_2255365, 257 citations [M,H]
 rabbit anti-TBR1 (Abcam ab31940), RRID:AB_2200219, 329 citations [M,H]
 chicken anti-TBR2 (EOMES; EMD Millipore AB15894), RRID:AB_10615604, 52 citations [M,H]
 rabbit anti-tubulin B3 (TUBB3, BioLegend, 802001), RRID:AB_2564645, 60 citations [M,H]
 guinea pig anti-VGAT (Synaptic Systems 131004) RRID:AB_887873, 144 citations [M,H]
 guinea pig anti-VGLUT1 (SLC17A7; EMD Millipore AB5905), RRID:AB_2301751, 451 citations [M,H]

Secondary Antibodies:

Fluorescein (FITC)-conjugated Donkey anti-Chicken IgY (Jackson Immunoresearch 703-095-155), RRID:AB_2340356, 48 citations
 Alexa Fluor 488-conjugated Donkey anti-Chicken IgY (Jackson Immunoresearch 703-545-155), RRID:AB_2340375, 357 citations
 Cy3-conjugated Donkey anti-Chicken IgY (Jackson Immunoresearch 703-165-155), RRID:AB_2340363, 63 citations
 Cy5-conjugated Donkey anti-Chicken IgY (Jackson Immunoresearch 703-175-155), RRID:AB_2340365, 22 citations
 Dylight 405-conjugated Donkey anti-Goat IgG (Jackson Immunoresearch 705-545-147), RRID:AB_2340426, 6 citations
 Alexa Fluor 488-conjugated Donkey anti-Goat IgG (Jackson Immunoresearch 705-545-147), RRID:AB_2336933, 156 citations
 Cy3-conjugated Donkey anti-Goat IgG (Jackson Immunoresearch 705-165-147), RRID:AB_2307351, 288 citations
 Alexa Fluor 594-conjugated Donkey anti-Goat IgG (Jackson Immunoresearch 705-585-147), RRID:AB_2340433, 50 citations
 Alexa Fluor 647-conjugated Donkey anti-Goat IgG (Jackson Immunoresearch 705-605-147), RRID:AB_2340437, 89 citations
 Fluorescein (FITC)-conjugated Donkey anti-Guinea Pig IgG (Jackson Immunoresearch 706-095-148), RRID:AB_2340453, 43 citations
 Alexa Fluor 488-conjugated Donkey anti-Guinea Pig IgG (Jackson Immunoresearch 706-545-148), RRID:AB_2340472, 130 citations
 Cy3-conjugated Donkey anti-Guinea Pig IgG (Jackson Immunoresearch 706-165-148), RRID:AB_2340460, 136 citations
 Alexa Fluor 594-conjugated Donkey anti-Guinea Pig IgG (Jackson Immunoresearch 706-585-148), RRID:AB_2340474, 36 citations
 Alexa Fluor 647-conjugated Donkey anti-Guinea Pig IgG (Jackson Immunoresearch 706-605-148), RRID:AB_2340476, 98 citations
 Dylight 405-conjugated Donkey anti-Mouse IgG (Jackson Immunoresearch 715-475-151), RRID:AB_2340840, 11 citations
 Alexa Fluor 488-conjugated Donkey anti-Mouse IgG (Jackson Immunoresearch 715-545-151), RRID:AB_2341099, 127 citations
 Cy3-conjugated Donkey anti-Mouse IgG (Jackson Immunoresearch 715-165-150), RRID:AB_2340813, 382 citations
 Cy3-conjugated Donkey anti-Mouse IgG (Jackson Immunoresearch 715-165-151), RRID:AB_2315777, 218 citations
 Alexa Fluor 647-conjugated Donkey anti-Guinea Pig IgG (Jackson Immunoresearch 715-605-150), RRID:AB_2340862, 122 citations
 Alexa Fluor 488 Goat anti-Mouse IgG1 Cross-Adsorbed (Invitrogen A21121), RRID:AB_2535764, 513 citations
 Alexa Fluor 594 Goat anti-Mouse IgG2a Cross-Adsorbed (Invitrogen A21135), RRID:AB_2535774, 55 citations
 Dylight 405-conjugated Donkey anti-Rabbit IgG (Jackson Immunoresearch 711-475-152), RRID:AB_2340616, 39 citations
 Alexa Fluor 488-conjugated Donkey anti-Rabbit IgG (Jackson Immunoresearch 711-545-152), RRID:AB_2313584, 558 citations
 Cy3-conjugated Donkey anti-Rabbit IgG (Jackson Immunoresearch 711-165-152), RRID:AB_2307443, 988 citations
 Alexa Fluor 594-conjugated Donkey anti-Rabbit IgG (Jackson Immunoresearch 711-585-152), RRID:AB_2340621, 230 citations
 Alexa Fluor 647-conjugated Donkey anti-Rabbit IgG (Jackson Immunoresearch 711-605-152), RRID:AB_2492288, 287 citations
 Alexa Fluor 488-conjugated Donkey anti-Rat IgG (Jackson Immunoresearch 712-545-153), RRID:AB_2340684, 57 citations
 Cy3-conjugated Donkey anti-Rat IgG (Jackson Immunoresearch 712-165-153), RRID:AB_2340667, 179 citations
 Alexa Fluor 594-conjugated Donkey anti-Rat IgG (Jackson Immunoresearch 712-585-153), RRID:AB_2340689, 13 citations
 Alexa Fluor 647-conjugated Donkey anti-Rat IgG (Jackson Immunoresearch 712-605-153), RRID:AB_2340694, 91 citations
 Fluorescein (FITC)-conjugated Donkey anti-Sheep IgG (Jackson Immunoresearch 713-095-147), RRID:AB_2340719, 23 citations
 Cy3-conjugated Donkey anti-Sheep IgG (Jackson Immunoresearch 713-165-147), RRID:AB_2315778, 37 citations
 Alexa Fluor 647-conjugated Donkey anti-Sheep IgG (Jackson Immunoresearch 713-605-147), RRID:AB_2340751, 16 citations

Eukaryotic cell lines

Policy information about [cell lines](#)

Cell line source(s)

H9 human embryonic stem cells were described by Thomson et al Science 282, 1145-1147, (1998), and received from the UCLA Broad Stem Cell Research Center Stem Cell core. Both Rett patient iPSC (wild-type and MECP2-deficient) were generated in the laboratories of Drs. Kathrin Plath and William Lowry, and were described by Ohashi et al. Stem Cell Reports 10, 1453-1463, (2018).

Authentication

The H9 stem cells were routinely karyotyped by the UCLA Broad Stem Cell Research Center Stem Cell core. Both Rett patients hiPSC were authenticated with respect to their MECP2 mutant status by Ohashi et al. Stem Cell Reports 10, 1453-1463 (2018) by immunoblotting and immunostaining for MECP2 protein expression, RNA-Seq analyses, genomic methylation analyses, differentiation into neurons in 2D culture with characterization of neuronal defects, and teratoma assays to confirm multipotency of the iPSC line. We similarly perform immunohistochemical analyses to confirm MECP2 mutant status of the iPSC and differentiated organoids as reported in this manuscript.

Mycoplasma contamination

All cell lines tested negative for mycoplasma contamination.

Commonly misidentified lines (See [ICLAC](#) register)

No misidentified lines were used in the study.